npj | computational materials

Article

Published in partnership with the Shanghai Institute of Ceramics of the Chinese Academy of Sciences

https://doi.org/10.1038/s41524-025-01821-0

Systematic cRPA study of two-dimensional MA_2Z_4 materials: from unconventional screening to correlation-driven instabilities

F. Bagherpour[1], Y. Yekta[1], H. Hadipour[1] ✉, E. Şaşıoğlu[2] ✉, A. Khademi[3], S. A. Jafari[4], I. Mertig[2] & S. Lounis[2]

Understanding the interplay between screening, electronic correlations, and collective excitations is essential for the design of two-dimensional quantum materials. Here, we present a comprehensive first-principles study of more than 60 MA_2Z_4 monolayers, encompassing semiconducting, metallic, cold-metallic, magnetic, and topological phases. Using the constrained random phase approximation (cRPA), we compute material-specific effective Coulomb interaction parameters U, U', and J, including their spatial dependence across distinct correlated subspaces defined by local coordination and crystal symmetry. In semiconducting compounds, long-range nonlocal interactions persist, revealing unconventional screening and suggesting strong excitonic effects beyond simple dielectric models. In cold-metallic systems, sizable long-range Coulomb interactions remain despite the presence of free carriers, highlighting their atypical metallic screening. Among 33-valence-electron compounds, we find $U^{\text{eff}} > W$ in the β_2 phase, indicating proximity to charge-density-wave or Mott instabilities. Several V- and Nb-based systems exhibit intermediate-to-strong correlation strength, with $U/W > 1$ in multiple cases. Using cRPA-derived Stoner parameters, we identify magnetic instabilities in various V-, Nb-, Cr-, and Mn-based compounds. Finally, selected cold-metallic systems display plasmon dispersions that deviate from the conventional $\sqrt{q}$ behavior, revealing nearly non-dispersive low-energy modes. These results position MA_2Z_4 monolayers as a versatile platform for investigating correlation-driven instabilities and emergent collective behavior in two dimensions.

Two-dimensional (2D) materials have reshaped the landscape of condensed matter physics and nanotechnology, providing an ideal platform to explore quantum phenomena in reduced dimensions[1,2]. Their atomically thin geometry leads to modified dielectric screening, tunable electronic properties, and access to a rich spectrum of correlation-driven and collective phases. Beyond their applications in electronics and optoelectronics, 2D materials have emerged as a promising platform for strongly correlated phenomena such as Mott insulating behavior[3], quantum spin liquids[4], and flat-band superconductivity[5]. In many such systems, electron-electron interactions dominate over single-particle band effects, making it essential to understand not only the strength but also the spatial dependence of Coulomb interactions. These characteristics are strongly influenced by reduced dimensionality, dielectric environment, and orbital character, all of which modulate the screening behavior. Consequently, there is growing demand for first-principles frameworks capable of quantifying interaction parameters in 2D materials, particularly where conventional assumptions about screening no longer hold.

A fundamental factor governing correlation strength in low-dimensional systems is the nature of Coulomb screening. In 2D materials, the suppression of dielectric screening enhances its spatial nonlocality relative to bulk systems[6–8], resulting in long-range electron-electron interactions that significantly influence both quasiparticle excitations and collective modes. These unconventional screening characteristics underlie large exciton binding energies in semiconducting monolayers[9] and flattened plasmon dispersions in cold metallic 2D systems[10]. Moreover, reduced screening can amplify Coulomb repulsion, favoring magnetic order, Mott

[1]Department of Physics, University of Guilan, Rasht, Iran. [2]Institute of Physics, Martin Luther University Halle-Wittenberg, Halle (Saale), Germany. [3]Department of Physics, Sharif University of Technology, Tehran, Iran. [4]2nd Institute of Physics C, RWTH Aachen University, Aachen, Germany.
✉e-mail: hanifhadipour@gmail.com; ersoy.sasioglu@physik.uni-halle.de

transitions, or plasmonic instabilities. These considerations highlight the need for a material-specific understanding of screening and correlation effects to capture emergent phases and guide functional materials design.

A widely used method for determining electronic interactions from first principles is the constrained random phase approximation (cRPA)[11–15]. By decomposing the electronic polarization into low-energy (model) and high-energy (rest) contributions, cRPA enables the computation of partially screened Coulomb interactions, such as the on-site intra-orbital Hubbard U, inter-orbital interaction U', and exchange J that enter effective low-energy Hamiltonians. This approach has been successfully applied to a broad range of correlated materials, including transition metal oxides[16], unconventional superconductors[17], and monolayer transition-metal dichalcogenides (TMDs)[18,19]. However, a systematic investigation of cRPA-derived interaction parameters in the recently discovered 2D MA_2Z_4 materials remains absent, despite the structural uniqueness and correlated ground states found in this class.

MA_2Z_4 monolayers represent a chemically and structurally diverse family of 2D materials that extend beyond traditional van der Waals systems[20,21]. Unlike most 2D materials derived from layered bulk crystals, MA_2Z_4 compounds, first realized via the synthesis of $MoSi_2N_4$, lack a known three-dimensional analogues. Their septuple-layer structure (Z-A-Z-M-Z-A-Z) combines a TMD-like MZ_2 slab with an intercalated A_2Z_2 layer, yielding high thermodynamic stability and intrinsic two-dimensionality. This architecture supports extensive chemical flexibility, with over 70 predicted stable monolayers across multiple structural symmetries ($\alpha, \beta, \gamma, \delta$, see few examples in Fig. 1) and electronic ground states. The MA_2Z_4 family hosts a wide range of electronic phases, including semiconductors, metals, cold metals, SGMs, spin-gapless semiconductors (SGSs), ferromagnets, and topological insulators, and exhibits properties such as ultrahigh carrier mobilities, large exciton binding energies, strain-tunable magnetism, and valley-selective optical responses[21–26]. Given this chemical and electronic diversity, a quantitative study of Coulomb interaction screening, correlation strength, and magnetic tendencies across the MA_2Z_4 family is both timely and essential for future theoretical and applied advances, particularly in the design of correlated 2D materials for spintronic, optoelectronic, and quantum information technologies.

In this work, we present a comprehensive first-principles investigation of screening behavior, Coulomb interaction parameters, correlation strength, and collective excitations across more than 60 MA_2Z_4 monolayers using the cRPA. We compute effective (partially screened) on-site interactions (U, U', and J) and their spatial dependence across different correlated subspaces defined by orbital character and local symmetry. In semiconducting compounds, we find that long-range nonlocal interactions persist, suggesting unconventional screening behavior and the relevance of strong excitonic effects beyond simple dielectric screening. In cold-metallic systems, sizable long-range interactions are found despite the presence of free carriers, highlighting their atypical metallic screening. Among 33-valence-electron systems, our analysis of on-site and off-site interactions in the β_2 phase reveals candidate materials for charge-density-wave (CDW) or Mott instabilities, with $U^{\text{eff}} > W$ in multiple cases. Several V- and Nb-based compounds exhibit intermediate-to-strong correlation strength ($U/W > 1$), and spin-polarized density-functional theory (DFT) calculations show finite magnetic moments. Applying the Stoner criterion with cRPA-derived Stoner parameters, we identify magnetic instabilities in various V-, Cr-, Nb-, and Mn-based compounds. Finally, for selected cold-metallic materials, we compute plasmon dispersions and observe deviations from the conventional $\sqrt{q}$ behavior, indicating the emergence of slow, nearly non-dispersive plasmon modes. Although explicit many-body corrections beyond DFT are not included, our results offer a rigorous, material-specific foundation for future DFT+DMFT or model Hamiltonian studies. The comprehensive dataset presented here serves as a reference for understanding correlation-driven phenomena and guiding the design of MA_2Z_4-based materials for applications in spintronics, excitonics, and plasmonics.

Results and discussion

The structural and electronic diversity of MA_2Z_4 monolayers, widely reported in the literature, motivates our systematic investigation of Coulomb interaction parameters and magnetic tendencies across this family. While all compounds share a common septuple-layer architecture, differences in atomic arrangement and symmetry give rise to multiple stable polytypes. Figure 1 shows representative low-energy configurations across the α_1, α_2, β_1, β_2, and β_5 structural classes, as identified in high-throughput studies and confirmed by phonon calculations[21]. Each phase exhibits a distinct coordination environment of the transition-metal atom, ranging from trigonal prismatic (1H-like) to ideal octahedral (1T-like), which modulates the crystal field splitting and influences the definition of the correlated subspace. We also include a representative CDW reconstructed β_2 structure to highlight possible symmetry-lowering effects in strongly correlated regimes. These structural motifs form the basis for selecting correlated orbitals in the subsequent cRPA analysis.

Correlated subspaces in 2D MA_2Z_4 materials

To compute screened Coulomb interactions within the cRPA framework, it is essential to define an appropriate correlated subspace for each

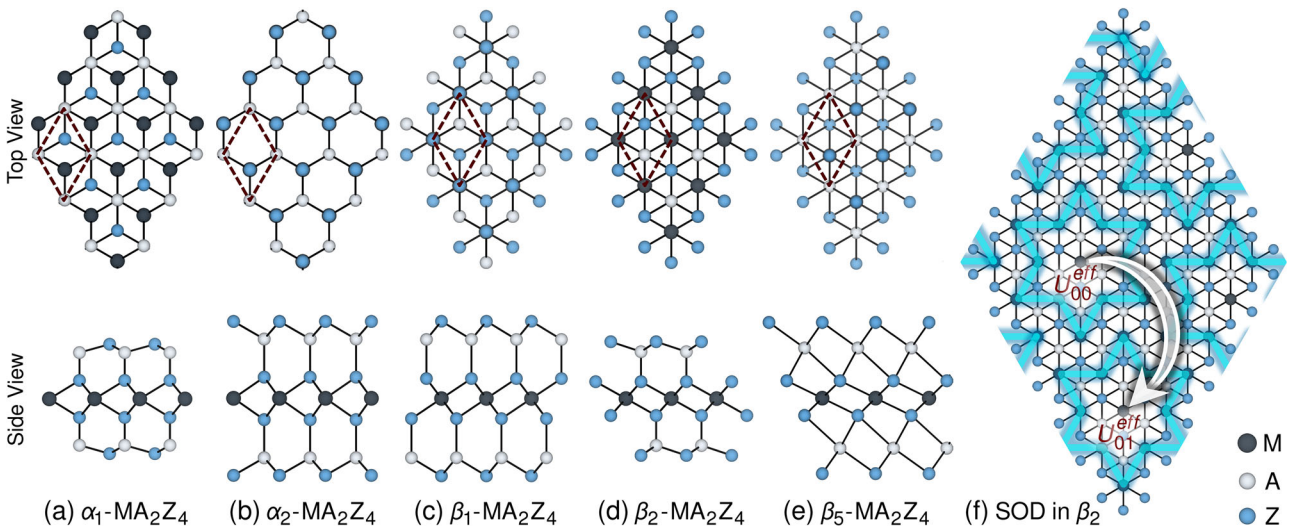

Fig. 1 | Crystal structures of representative MA_2Z_4 monolayers. Side and top views of the two-dimensional crystal structure of intercalated architecture MA_2Z_4 in **a** α_1 structure, **b** α_2 structure, **c** β_1 structure, **d** β_2 structure, **e** β_5 structure, and **f** Star-of-David (SOD) reconstructed β_2 crystal structure. Dark gray, white, and blue spheres denote M, A, and Z atoms, respectively.

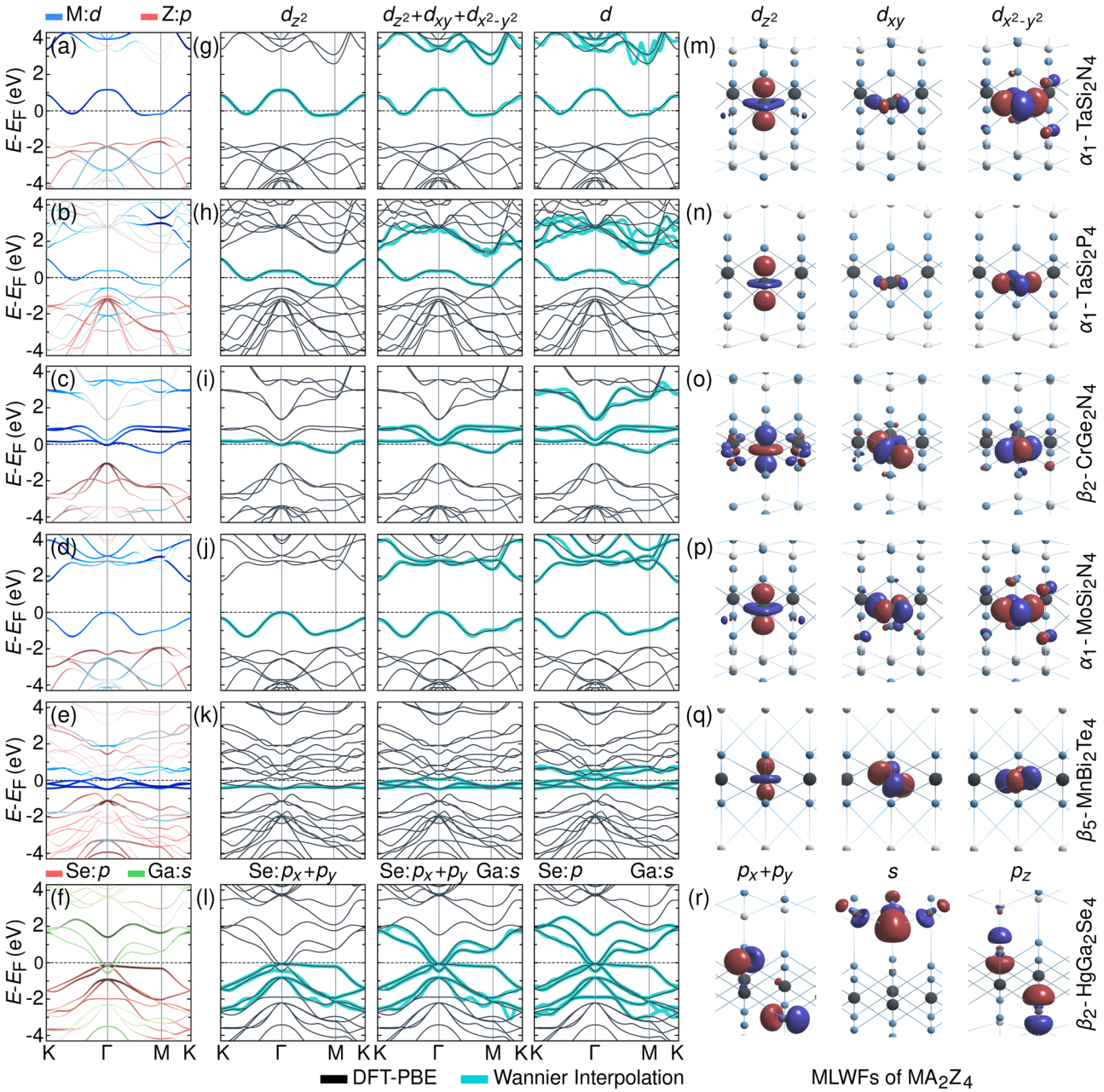

Fig. 2 | Electronic structure and maximally localized Wannier functions (MLWFs) for representative MA_2Z_4 compounds. a–f The projected DFT-PBE band structures of α_1-$TaSi_2N_4$, α_1-$TaSi_2P_4$, β_2-$CrGe_2N_4$, α_1-$MoSi_2N_4$, β_5-$MnBi_2Te_4$, and β_2-$HgGa_2Se_4$. **g–l** compare the original DFT-PBE bands (gray) with the Wannier-interpolated bands (cyan) for three different correlated subspaces. **m–r** display the spatial distributions of selected MLWFs used in the construction of these subspaces. Left column: d_{z^2}-like MLWF (one-orbital model). Middle column: d_{xy}-like MLWF from a three-orbital subspace ($d_{z^2} + d_{xy} + d_{x^2-y^2}$). Right column: $d_{x^2-y^2}$-like MLWF from the full d-manifold. For the topological compound β_2-$HgGa_2Te_4$, the relevant subspaces consist of p_x+p_y, $s + p_x$+p_y, and $s + p$ orbitals.

material. We identify this subspace based on the dominant orbital character near the Fermi level, as obtained from DFT calculations and maximally localized Wannier function (MLWF) analysis. Across the majority of MA_2Z_4 compounds, the low-energy electronic structure is primarily derived from the transition metal (M) d orbitals, with negligible contribution from A or Z atoms. This trend enables a consistent treatment using d-orbital-based correlated subspaces. Depending on the degree of band separation and orbital mixing, we construct MLWFs for one-, three-, and five-orbital models. Figure 2 illustrates the comparison between DFT and Wannier-interpolated bands, along with representative MLWF spatial profiles. Additional examples of Wannier interpolations and orbital-resolved character for different subspaces are provided in Supplementary Figs. S1–S3.

For semiconductors and cold metallic systems with isolated d_{z^2} bands crossing the Fermi level, such as α_1-$TaSi_2N_4$ and α_1-$NbSi_2P_4$, a one-orbital model is sufficient. In materials where additional d_{xy} and $d_{x^2-y^2}$ states contribute within a narrow energy window (e.g., α_1-$MoSi_2N_4$), a minimal three-orbital model offers a more accurate description. In more complex cases like β_2-$CrGe_2N_4$, where strong hybridization between d_{z^2} and other e_g orbitals occurs, the correlated subspace must be extended to include all five d orbitals. These subspace definitions enable a consistent treatment of electron correlation effects across the d-dominated MA_2Z_4 materials.

A notable exception to this d-orbital-based description arises in the 32-valence-electron MA_2Z_4 compounds. These systems, typically involving group-12 transition metals (e.g., Zn, Cd, Hg) combined with lighter A and Z atoms, feature low-energy states near the Fermi level that originate primarily

from *s* and *p* orbitals of the A and Z atoms, rather than from M-*d* states. For these *s*/*p*-dominated semiconductors, we construct two-, three-, and four-orbital correlated subspaces based on appropriate combinations of *s* and *p* orbitals. These models—illustrated in Fig. 2f, l, and r—are essential for accurately capturing correlation effects in non-*d*-like semiconducting phases.

The choice of correlated subspace influences the calculated interaction parameters and should reflect the physical properties of interest. Minimal models are sufficient for evaluating low-energy transport properties, while more complete subspaces are required for describing optical excitations or many-body instabilities. In the following sections, we report Coulomb interaction parameters for each material using one-orbital (d_{z^2}), three-orbital ($d_{z^2} + d_{xy} + d_{x^2-y^2}$ or $d_{z^2} + e_g$), and five-orbital (*d*-manifold) models, as well as *s*/*p*-based subspaces for the 32-valence-electron materials.

Coulomb interactions in 2D MA_2Z_4 with 32 and 34 valence electrons

We begin our quantitative analysis of Coulomb interactions with the 34-valence-electron MA_2Z_4 monolayers. This subset comprises a large number of semiconducting compounds based on Mo and W, along with a smaller set of Cr-based materials that display metallic or magnetic ground states. These systems are particularly relevant for understanding electronic correlation effects, as their low-energy states are dominated by transition-metal *d* orbitals. The prototypical $MoSi_2N_4$, the first experimentally synthesized member of the MA_2Z_4 family, also belongs to this class, making it a natural reference point for our analysis[20]. While on-site Coulomb interactions play a central role in local correlation physics, the long-range behavior of the interaction is equally crucial in 2D materials, where screening is reduced and non-local effects can become significant. To ensure consistency in the definition of interaction parameters and to simplify the construction of localized Wannier functions, all cRPA and RPA calculations are performed using a non-spin-polarized state, even for compounds that exhibit magnetic ordering in spin-polarized calculations. This choice preserves spin symmetry, avoids complications related to spin-dependent screening channels, and prevents spurious screening effects introduced by broken-symmetry DFT states. It also aligns with the formal structure of many-body techniques such as DFT+DMFT or model Hamiltonian approaches, in which magnetic fluctuations are treated dynamically and self-consistently within the correlated subspace.

As a first step, we examine the bare intra-orbital Coulomb interaction *V*, which provides a measure of the spatial localization of the underlying Wannier orbitals. Table 1 and Fig. 3 show that *V* varies substantially across the MA_2Z_4 family, spanning a range from ~4 to 16 eV depending on chemical composition, lattice structure, and the choice of correlated subspace. Across all compounds, we find that Cr-based systems exhibit the largest *V* values, consistent with the stronger localization of 3*d* orbitals relative to their 4*d* (Mo) and 5*d* (W) counterparts. In parallel, a clear anion trend is observed: for a fixed transition metal and cation, the bare interaction decreases as the anion changes from N to P to As. This trend reflects the increased lattice spacing and weaker hybridization associated with heavier anions, both of which contribute to more delocalized Wannier functions. The influence of cation substitution (Si vs. Ge) is more subtle but generally results in a modest reduction of *V*, likely due to lattice expansion and altered bonding geometry. Overall, the observed variations in *V* highlight the strong sensitivity of orbital localization to both electronic and structural degrees of freedom.

In addition to these chemical trends, *V* exhibits a systematic dependence on the size of the correlated subspace. In particular, the one-orbital (d_{z^2}) model yields the lowest *V*, the three-orbital (d_{z^2}, d_{xy}, and $d_{x^2-y^2}$) model gives a significantly higher value, and the five-orbital (*d*) model produces a *V* that is slightly smaller than in the three-orbital case. The reduced *V* in the 1-orbital subspace reflects the strong delocalization of the isolated Wannier orbital, which is more extended due to the lack of nearby states within the same manifold. Conversely, the slight drop in *V* for the five-orbital case relative to the three-orbital model can be attributed to enhanced delocalization arising from metal–ligand (*p*–*d*) hybridization. This consistent trend across the 34-electron MA_2Z_4 series reveals how the choice of correlated subspace influences Wannier function localization and, consequently, the strength of the bare Coulomb interaction *V*.

To quantify the effects of screening, we compute the effective (partially screened) Coulomb interaction parameters, namely the intra-orbital Hubbard interaction *U*, the inter-orbital interaction *U*′, and the exchange interaction *J*, within the cRPA, which excludes screening contributions from the low-energy correlated subspace. Additionally, we evaluate the fully screened interactions $\tilde{U}$, $\tilde{U}'$, and $\tilde{J}$ using the full random phase approximation (RPA), which includes all electronic transitions. Table 1 provides a comprehensive dataset of Coulomb parameters for all 34-valence-electron MA_2Z_4 compounds, evaluated for three different correlated subspaces. These results are further contextualized in Fig. 3, which displays the intra-orbital *V*, *U*, and $\tilde{U}$ values not only for the 34-electron subset but also across the broader set of MA_2Z_4 compounds with 32, 33, and 41 valence electrons. The full 3×3 and 5×5 cRPA Coulomb matrices for all 34-electron compounds are provided in the Supplementary Material, enabling more detailed many-body modeling beyond the averaged values discussed here.

In the semiconducting Mo- and W-based compounds, the partially screened Hubbard–Kanamori interaction *U* ranges from 0.5 to 3.2 eV, depending on the correlated subspace and chemical environment. These values are comparable to or larger than those reported for other 2D semiconductors such as MoS_2[18,27], consistent with reduced dielectric screening in low-dimensional systems. Notably, *U* increases along the transition-metal series from Cr to Mo to W, reflecting the interplay between orbital character and screening efficiency. This trend is indicative of weaker *p*-to-*d* screening in heavier transition metals, where larger band gaps reduce the effectiveness of polarization screening from ligand states. For example, in the full *d*-orbital subspace, the interaction *U* increases from 1.38 eV in $MoGe_2P_4$ to 2.85 eV in WGe_2N_4. Anion substitution also plays a significant role: within the $MoSi_2Z_4$ series, the interaction *U* decreases from 3.12 eV in $MoSi_2N_4$ to 1.57 eV in $MoSi_2P_4$, and further to 1.53 eV in $MoSi_2As_4$, reflecting the enhanced screening in compounds with heavier anions and wider lattice constants. A similar trend is observed in the W-based series, with *U* in the full-*d* subspace decreasing from 3.08 eV in WSi_2N_4 to 1.50 eV in WSi_2P_4, and 1.34 eV in WSi_2As_4. Comparing Si- and Ge-based compounds reveals a more nuanced effect: while lattice expansion associated with Ge substitution tends to slightly reduce *U*, the trend is not always monotonic. For instance, WSi_2N_4 and WGe_2N_4 exhibit similar values of *U* (3.08 eV vs. 2.85 eV), suggesting that structural and hybridization effects can partially compensate for the expected increase in screening. Overall, these trends reveal the subtle interplay between chemical composition, orbital character, and lattice geometry in determining the effective strength of electron-electron interactions in the MA_2Z_4 family.

To gain deeper insight into the nature of screening in MA_2Z_4 materials, we extend our analysis beyond the on-site limit and examine the real-space decay of the intra-orbital Coulomb interaction $U(r)$. Understanding the spatial profile of $U(r)$ is essential for assessing the range and strength of electron-electron interactions, particularly in 2D systems where non-local screening effects are pronounced. In the following, we focus on representative compounds from the 34-valence-electron family to explore how screening behavior evolves with electronic structure, dimensionality, and material composition. These results reveal substantial differences between semiconducting and metallic systems. Complete long-range interaction data, including $U(r)$ values up to the sixth nearest neighbor for all 34-electron compounds and all correlated subspaces, are provided in Table S1 in the Supplementary Material.

The long-range behavior of the Coulomb interaction is particularly revealing in the case of semiconductors, where reduced dimensionality suppresses conventional dielectric screening. As shown in Fig. 4, we plot the real-space decay of the bare, partially screened, and fully screened intra-orbital Coulomb interactions—$V(r)$, $U(r)$, and $\tilde{U}(r)$—for the representative compounds α_1-$MoSi_2N_4$, α_1-WSi_2N_4, and spin-gapped metal (SGM) β_2-$CrGe_2N_4$. In all cases, *r* is expressed in units of the in-plane lattice constant *a*. For the semiconducting systems, we observe a pronounced deviation from conventional metallic or bulk-like screening behavior. In α_1-$MoSi_2N_4$, shown in panel (a), the effective interaction $U(r)$ remains substantial up to at

Table 1 | Crystal symmetry, lattice parameter, electronic ground state, correlated subspace, and Coulomb interaction parameters for *d* orbitals of transition-metal atoms in 2D MA_2Z_4 compounds with 34 valence electrons (M = Cr, Mo, W; A = Si, Ge; Z = N, P, As)

MA_2Z_4	Phase	a (Å)	Ground State	Correlated Subspace	V (eV)	U (eV)	U' (eV)	J (eV)	$\tilde{U}$ (eV)	$\tilde{U}'$ (eV)	$\tilde{J}$ (eV)
$CrSi_2N_4$	α_1	2.84	SC	d_{z^2}	9.00	1.25	–	–	1.25	–	–
				$d_{z^2}+d_{xy}+d_{x^2-y^2}$	15.37	3.28	2.40	0.48	1.97	1.31	0.35
				d	14.52	3.15	2.54	0.39	2.00	1.42	0.30
$CrSi_2P_4$	α_2	3.41	SC	d_{z^2}	7.60	0.71	–	–	0.71	–	–
				$d_{z^2}+d_{xy}+d_{x^2-y^2}$	14.00	2.01	1.27	0.38	1.26	0.72	0.28
				d	12.44	1.82	1.33	0.30	1.23	0.78	0.24
$CrSi_2As_4$	β_1	3.68	FM	d_{z^2}	5.81	0.26	–	–	0.26	–	–
				$d_{z^2}+e_g$	13.09	1.10	0.49	0.30	0.61	0.23	0.18
				d	11.96	1.07	0.65	0.25	0.63	0.29	0.17
$CrGe_2N_4$	β_2	3.06	SGM	d_{z^2}	8.96	0.57	–	–	0.57	–	–
				$d_{z^2}+e_g$	15.83	3.22	2.34	0.44	0.98	0.49	0.20
				d	15.64	2.69	1.96	0.42	1.17	0.54	0.24
$CrGe_2P_4$	α_2	3.49	SC	d_{z^2}	7.49	0.65	–	–	0.63	–	–
				$d_{z^2}+d_{xy}+d_{x^2-y^2}$	14.11	1.91	1.20	0.36	1.14	0.64	0.26
				d	12.47	1.73	1.27	0.27	1.10	0.69	0.22
$CrGe_2As_4$	β_1	3.78	FM	d_{z^2}	4.00	0.24	–	–	0.23	–	–
				$d_{z^2}+e_g$	7.45	0.70	0.33	0.10	0.55	0.25	0.09
				d	7.00	0.65	0.35	0.08	0.51	0.26	0.07
$MoSi_2N_4$	α_1	2.91	SC	d_{z^2}	7.11	1.42	–	–	1.42	–	–
				$d_{z^2}+d_{xy}+d_{x^2-y^2}$	10.54	3.16	2.58	0.33	2.23	1.71	0.29
				d	10.41	3.12	2.69	0.27	2.26	1.80	0.25
$MoSi_2P_4$	α_2	3.46	SC	d_{z^2}	4.13	0.60	–	–	0.58	–	–
				$d_{z^2}+d_{xy}+d_{x^2-y^2}$	8.80	1.67	1.23	0.24	1.29	0.88	0.21
				d	8.13	1.57	1.26	0.19	1.13	0.94	0.12
$MoSi_2As_4$	α_2	3.61	SC	d_{z^2}	4.00	0.51	–	–	0.51	–	–
				$d_{z^2}+d_{xy}+d_{x^2-y^2}$	9.77	1.66	1.14	0.28	1.25	0.78	0.24
				d	8.82	1.53	1.17	0.22	1.18	0.83	0.20
$MoGe_2N_4$	α_1	3.02	SC	d_{z^2}	7.18	1.28	–	–	1.28	–	–
				$d_{z^2}+d_{xy}+d_{x^2-y^2}$	9.70	2.73	2.21	0.29	1.89	1.43	0.25
				d	10.36	2.88	2.45	0.27	2.05	1.59	0.24
$MoGe_2P_4$	α_2	3.53	SC	d_{z^2}	5.14	0.65	–	–	0.65	–	–
				$d_{z^2}+d_{xy}+d_{x^2-y^2}$	8.84	1.59	1.14	0.23	1.21	0.81	0.20
				d	8.28	1.38	1.18	0.12	1.07	0.88	0.11
$MoGe_2As_4$	α_2	3.69	SC	d_{z^2}	5.28	0.58	–	–	0.56	–	–
				$d_{z^2}+d_{xy}+d_{x^2-y^2}$	9.61	1.59	1.08	0.27	1.18	0.72	0.23
				d	8.84	1.36	1.13	0.14	1.02	0.79	0.13
WSi_2N_4	α_1	2.91	SC	d_{z^2}	6.85	1.48	–	–	1.48	–	–
				$d_{z^2}+d_{xy}+d_{x^2-y^2}$	9.90	3.19	2.65	0.33	2.34	1.83	0.29
				d	9.43	3.08	2.69	0.27	2.31	1.89	0.25
WSi_2P_4	α_2	3.46	SC	d_{z^2}	4.94	0.70	–	–	0.70	–	–
				$d_{z^2}+d_{xy}+d_{x^2-y^2}$	8.19	1.65	1.24	0.23	1.30	0.91	0.21
				d	7.40	1.50	1.21	0.18	1.10	0.94	0.10
WSi_2As_4	α_2	3.61	SC	d_{z^2}	4.95	0.61	–	–	0.59	–	–
				$d_{z^2}+d_{xy}+d_{x^2-y^2}$	8.63	1.57	1.12	0.25	1.21	0.80	0.22
				d	7.92	1.34	1.16	0.12	1.04	0.86	0.11
WGe_2N_4	α_1	3.02	SC	d_{z^2}	6.84	1.32	–	–	1.32	–	–
				$d_{z^2}+d_{xy}+d_{x^2-y^2}$	9.53	2.87	2.33	0.30	2.05	1.55	0.26

Table 1 (continued) | Crystal symmetry, lattice parameter, electronic ground state, correlated subspace, and Coulomb interaction parameters for *d* orbitals of transition-metal atoms in 2D MA_2Z_4 compounds with 34 valence electrons (M = Cr, Mo, W; A = Si, Ge; Z = N, P, As)

MA_2Z_4	Phase	a (Å)	Ground State	Correlated Subspace	V (eV)	U (eV)	U' (eV)	J (eV)	$\tilde{U}$ (eV)	$\tilde{U}'$ (eV)	$\tilde{J}$ (eV)
				d	9.44	2.85	2.44	0.26	2.09	1.65	0.24
WGe_2P_4	α_2	3.54	SC	d_{z^2}	5.08	0.67	–	–	0.67	–	–
				$d_{z^2}+d_{xy}+d_{x^2-y^2}$	8.50	1.65	1.19	0.23	1.27	0.85	0.21
				d	7.68	1.38	1.21	0.11	1.07	0.90	0.10
WGe_2As_4	α_2	3.69	SC	d_{z^2}	5.05	0.55	–	–	0.54	–	–
				$d_{z^2}+d_{xy}+d_{x^2-y^2}$	8.88	1.54	1.05	0.25	1.16	0.72	0.22
				d	8.16	1.30	1.10	0.12	0.99	0.79	0.11

Listed are the bare intra-orbital interaction V, the partially screened Hubbard–Kanamori parameters [U, U', J], and the fully screened counterparts [$\tilde{U}$, $\tilde{U}'$, $\tilde{J}$]. For each compound, results are provided for three different correlated subspaces: a single-orbital model (d_{z^2}), a three-orbital model ($d_{z^2}+d_{xy}+d_{x^2-y^2}$, or $d_{z^2}+e_g$), and the full d-orbital manifold. Lattice parameters are taken from ref. 21. Abbreviations: SC — semiconductor; SGM — spin-gapped metal; FM — ferromagnet.

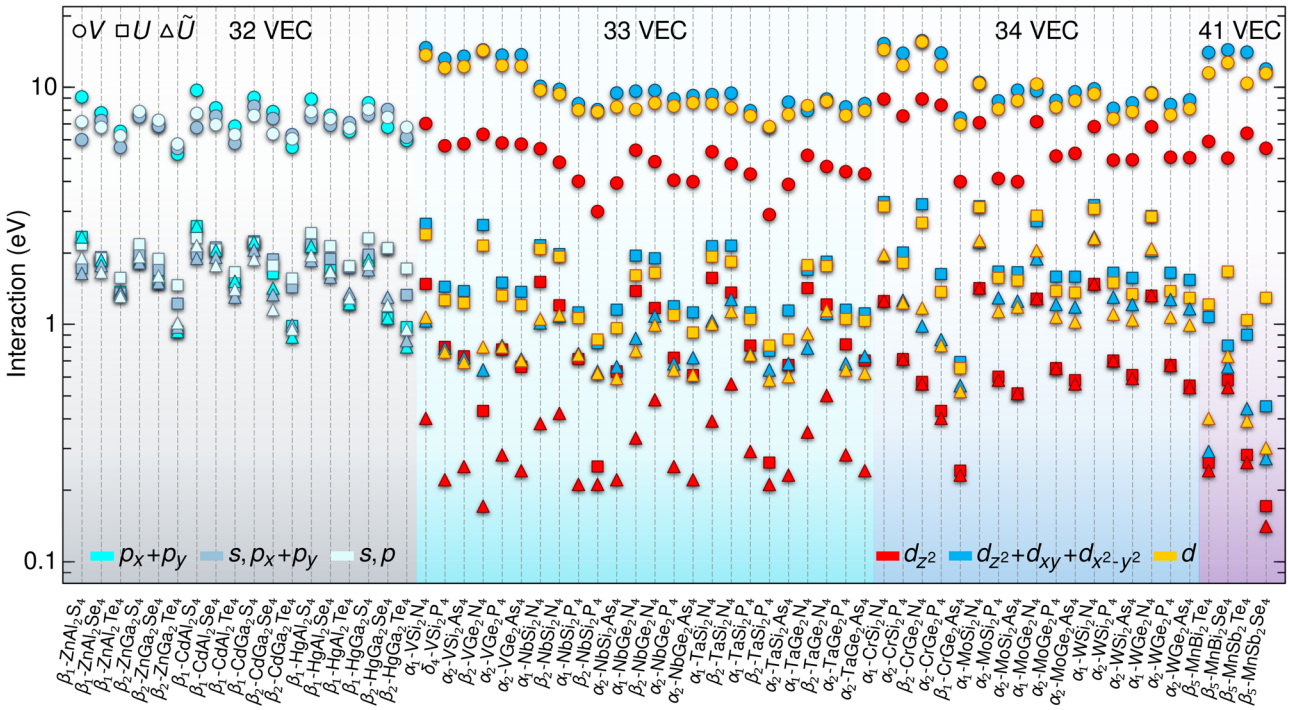

Fig. 3 | On-site intra-orbital Coulomb interaction parameters (V, U, and $\tilde{U}$) for 2D MA_2Z_4 compounds with 32, 33, 34, and 41 valence electrons. Results are shown for different correlated subspaces, enabling comparison of the strength and screening of electronic interactions across a wide range of chemical compositions and electronic configurations. The abbreviation VEC refers to valence electron count.

least 6a, and its long-range tail persists even at 20a [panel (b)]. A power-law fit reveals that $U(r) \sim r^{-0.6}$ and $\tilde{U}(r) \sim r^{-0.55}$, in stark contrast to the bare $V(r) \sim 1/r$ decay. This unusually slow screening reveals the nonlocal character of Coulomb interactions in 2D semiconductors.

A similar trend is found for α_1-WSi_2N_4 [panel (c)], where $U(r)$ and $\tilde{U}(r)$ exhibit nearly identical decay profiles to those in $MoSi_2N_4$, albeit without fitted exponents. The persistence of long-range interactions in both cases reveals a key feature of semiconducting MA_2Z_4 systems: the dielectric screening is strongly distance-dependent and cannot be captured by a simple static dielectric constant ϵ. For example, in α_1-$MoSi_2N_4$, the effective dielectric ratio $\epsilon(r) = V(r)/U(r)$ decreases with increasing distance, taking values of $\epsilon(a) \approx 2.8$, $\epsilon(2a) \approx 2.1$, and $\epsilon(3a) \approx 1.8$. This non-monotonic screening response indicates that long-range interactions are weakly screened and that $U(r)$ and $\tilde{U}(r)$ do not follow a conventional $1/\epsilon r$ form.

In contrast, the SGM β_2-$CrGe_2N_4$ [panel (d)] shows a much more localized interaction profile. Here, the screened Coulomb interaction decays rapidly and becomes negligible beyond approximately 6a, reflecting the stronger screening expected in metallic systems. This behavior is consistent with the emergence of delocalized carriers that effectively suppress long-range components of the Coulomb potential. Extended data for other metallic compounds, including off-site $U(r)$ values up to 6a, are provided in Table I of the Supplementary Material.

Overall, these results highlight the unconventional nature of screening in semiconducting MA_2Z_4 monolayers. The persistence of nonlocal Coulomb interactions over several lattice spacings, as seen in both the partially screened $U(r)$ and fully screened $\tilde{U}(r)$, has important implications for electronic and optical properties. In particular, the long-range behavior of $\tilde{U}(r)$ provides a microscopic basis for the large exciton binding energies and non-Rydberg excitonic series reported in $MoSi_2N_4$ and related

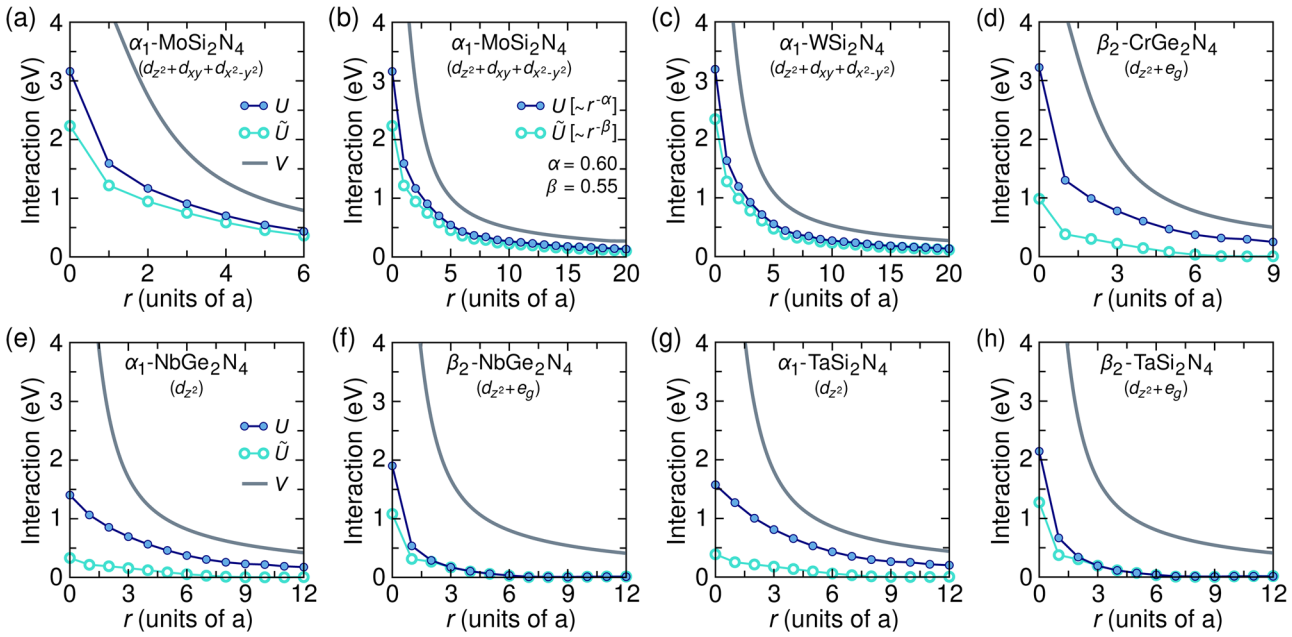

Fig. 4 | Real-space decay of the intra-orbital Coulomb interaction for selected MA_2Z_4 compounds with 34 and 33 valence electrons. Shown are the bare interaction $V(r)$ (solid lines), the partially screened interaction $U(r)$, and the fully screened interaction $\tilde{U}(r)$ as functions of distance r, expressed in units of the in-plane lattice constant a. All results correspond to the $d_{z^2}+d_{xy}+d_{x^2-y^2}$ (or $d_{z^2}+e_g$) correlated subspace. Present 34-valence-electron compounds: **a** displays $V(r)$, $U(r)$, and $\tilde{U}(r)$ for α_1-$MoSi_2N_4$ up to $r = 6a$; **b** extends this analysis to $r = 20a$ and includes power-law fits, where $U(r) \sim r^{-\alpha}$ and $\tilde{U}(r) \sim r^{-\beta}$ with $\alpha = 0.6$ and $\beta = 0.55$, respectively; **c** shows the analogous decay for α_1-WSi_2N_4 up to $r = 20a$, exhibiting a similar slow screening behavior without fitted exponents; **d** presents β_2-$CrGe_2N_4$ up to $r = 9a$, where the faster decay of $\tilde{U}(r)$ reflects stronger metallic screening. Extend the analysis to 33-valence-electron compounds: **e** and **f** show the decay of $V(r)$, $U(r)$, and $\tilde{U}(r)$ up to $r = 12a$ for α_1- and β_2-$NbGe_2N_4$, respectively; **g** and **h** present the corresponding results for α_1- and β_2-$TaSi_2N_4$ up to $r = 12a$.

materials[20,28,29]. While excitonic properties are not computed in this work, our analysis of distance-dependent screening establishes key input parameters for many-body calculations and supports the predictive design of MA_2Z_4-based optoelectronic and excitonic devices.

In light of these findings, the calculated off-site Coulomb interaction values, presented in Table I of the Supplementary Material, offer a valuable foundation for first-principles methods that go beyond purely local correlation models. In particular, the DFT+U+V framework, which supplements on-site Hubbard interactions with non-local intersite terms V, has proven effective in describing semiconductors with strong covalent bonding[30,31]. Given the covalently bonded in-plane structure of MA_2Z_4 monolayers and the persistence of long-range interactions observed in our calculations, especially for semiconducting compounds, DFT+U+V emerges as a natural candidate for improved electronic structure modeling in this class of materials. The distance-resolved $U(r)$ values provided here can serve as physically motivated input parameters for such extended Hubbard models, enabling future studies to better capture the interplay between short- and long-range correlation effects in 2D semiconductors.

While the primary focus of this work has been on 34-valence-electron MA_2Z_4 monolayers with d-orbital-dominated correlated subspaces, it is also important to consider the complementary class of materials with 32 valence electrons. In these systems, where M = Zn, Cd, or Hg, the low-energy electronic structure is primarily composed of s and p states, which are typically regarded as weakly correlated due to their spatially extended nature and reduced Coulomb repulsion. Nonetheless, several compounds in this class exhibit semimetallic or even topologically nontrivial features that make their screening properties particularly intriguing. Our cRPA calculations reveal that, despite their weaker on-site interactions, these systems often exhibit non-negligible long-range Coulomb interactions, especially in the β-phase structures. For example, in β_2-$CdGa_2Se_4$, the sixth-neighbor interaction reaches 0.26 eV, exceeding that of some semiconducting α-phase systems with d orbitals (see Table S3 in the Supplementary Material).

To provide a comprehensive reference for future studies, we include in Table S2 of the Supplementary Information the effective (partially screened) Coulomb parameters U, U', and J, as well as their fully screened counterparts $\tilde{U}$, $\tilde{U}$, and $\tilde{J}$, evaluated for multiple correlated subspaces in the 32-valence-electron systems. In Table S3, we further present distance-resolved off-site Coulomb interactions $U(r)$ up to the sixth nearest neighbor. These data confirm that long-range interactions in sp-electron semimetals can be significant and underscore the potential relevance of nonlocal correlation effects in these systems.

Coulomb interactions in 33-valence electron compounds

We now turn to the class of MA_2Z_4 compounds with 33 valence electrons, where M = V, Nb, or Ta; A = Si or Ge; and Z = N, P, or As. These materials exhibit a diverse range of electronic ground states, including SGSs, SGMs, and cold metals (see Fig. S4 in the Supplementary Information) characterized by a narrow half-filled band crossing the Fermi level[22,23,32–34]. This narrow-band feature is often indicative of enhanced electronic correlations, although a detailed analysis of correlation strength in terms of the ratio U/W will be presented in a separate subsection. A notable distinction arises in their magnetic character: V-based systems tend to favor magnetically ordered ground states and frequently realize SGS or SGM phases, whereas Nb- and Ta-based compounds are predominantly nonmagnetic and typically exhibit p-type or pn-type cold metallic behavior[21,35,36]. A few exceptions exist, notably α_1-$NbSi_2N_4$, α_1-$NbGe_2N_4$, and α_1-$TaGe_2N_4$, which display small exchange splittings and feature well-defined gaps above and below the Fermi level (see Fig. S5 in the Supplementary Information). These systems are classified as SGMs, or equivalently, magnetic cold metals.

To determine the Coulomb interactions in these systems, we perform cRPA and full RPA calculations using a non-magnetic reference state for all compounds, considering three correlated subspaces: the d_{z^2} orbital, a three-orbital set ($d_{z^2} + d_{xy} + d_{x^2-y^2}$), and the full d-manifold. The resulting interaction parameters are summarized in Table 2, which also indicates the magnetic ground state of each compound for completeness. This consistent dataset provides a basis for comparing with the 34-valence-electron systems

Table 2 | Crystal symmetry, lattice parameter, ground state, correlated subspace, bare Coulomb interaction V, partially screened Hubbard–Kanamori parameters [U, U', J], fully screened counterparts [$\tilde{U}$, $\tilde{U}'$, $\tilde{J}$] (in eV) for d orbitals of TMs in MA_2Z_4 (M=V, Nb, Ta; A=Si, Ge; Z=N, P, As) compounds

MA_2Z_4	Phase	a (Å)	Ground State	Correlated Subspace	V (eV)	U (eV)	U' (eV)	J (eV)	$\tilde{U}$ (eV)	$\tilde{U}'$ (eV)	$\tilde{J}$ (eV)
VSi_2N_4	α_1	2.88	SGS (type-II)	d_{z^2}	7.06	1.48	–	–	0.40	–	–
				$d_{z^2}+d_{xy}+d_{x^2-y^2}$	14.79	2.66	1.81	0.46	1.03	0.45	0.29
				d	13.76	2.40	1.84	0.37	1.07	0.51	0.27
VSi_2P_4	δ_4	3.48	SGS (type-II)	d_{z^2}	5.68	0.80	–	–	0.22	–	–
				$d_{z^2}+d_{xy}+d_{x^2-y^2}$	13.29	1.44	0.75	0.36	0.79	0.31	0.25
				d	12.15	1.26	0.77	0.28	0.76	0.34	0.21
VSi_2As_4	α_2	3.64	SGS (type-I)	d_{z^2}	5.79	0.73	–	–	0.25	–	–
				$d_{z^2}+d_{xy}+d_{x^2-y^2}$	13.60	1.38	0.67	0.37	0.72	0.25	0.24
				d	12.30	1.23	0.73	0.28	0.73	0.29	0.21
VGe_2N_4	β_2	3.05	SGM (pn-type)	d_{z^2}	6.35	0.43	–	–	0.17	–	–
				$d_{z^2}+e_g$	14.48	2.63	1.86	0.39	0.64	0.16	0.22
				d	14.38	2.15	1.51	0.37	0.80	0.21	0.25
VGe_2P_4	α_2	3.56	SGM (pn-type)	d_{z^2}	5.84	0.78	–	–	0.28	–	–
				$d_{z^2}+d_{xy}+d_{x^2-y^2}$	13.75	1.50	0.77	0.37	0.81	0.30	0.26
				d	12.42	1.32	0.81	0.29	0.80	0.35	0.23
VGe_2As_4	α_2	3.72	SSM	d_{z^2}	5.77	0.66	–	–	0.24	–	–
				$d_{z^2}+d_{xy}+d_{x^2-y^2}$	13.80	1.37	0.65	0.37	0.71	0.23	0.24
				d	12.33	1.20	0.69	0.28	0.71	0.28	0.21
$NbSi_2N_4$	α_1	2.96	SGM (pn-type)	d_{z^2}	5.52	1.51	–	–	0.38	–	–
				$d_{z^2}+d_{xy}+d_{x^2-y^2}$	10.15	2.16	1.62	0.31	1.01	0.55	0.24
				d	9.76	2.08	1.70	0.26	1.05	0.61	0.22
$NbSi_2P_4$	α_1	3.53	Cold-Metal (p-type)	d_{z^2}	4.02	0.71	–	–	0.21	–	–
				$d_{z^2}+d_{xy}+d_{x^2-y^2}$	8.56	1.12	0.70	0.23	0.75	0.38	0.19
				d	8.06	1.06	0.74	0.19	0.74	0.41	0.17
$NbSi_2As_4$	α_2	3.68	Cold-Metal (p-type)	d_{z^2}	3.95	0.63	–	–	0.22	–	–
				$d_{z^2}+d_{xy}+d_{x^2-y^2}$	9.50	1.15	0.65	0.27	0.66	0.33	0.18
				d	8.30	0.96	0.62	0.19	0.59	0.37	0.11
$NbGe_2N_4$	α_1	3.09	SGM (pn-type)	d_{z^2}	5.44	1.38–		–	0.33	–	–
				$d_{z^2}+d_{xy}+d_{x^2-y^2}$	9.68	1.95	1.43	0.29	0.87	0.45	0.21
				d	8.10	1.61	1.33	0.22	0.77	0.45	0.18
$NbGe_2P_4$	α_2	3.62	Cold-Metal (p-type)	d_{z^2}	4.06	0.72	–	–	0.25	–	–
				$d_{z^2}+d_{xy}+d_{x^2-y^2}$	8.98	1.19	0.72	0.24	0.67	0.37	0.16
				d	8.36	1.09	0.76	0.20	0.64	0.43	0.11
$NbGe_2As_4$	α_2	3.77	Cold-Metal (p-type)	d_{z^2}	4.00	0.61	–	–	0.22	–	–
				$d_{z^2}+d_{xy}+d_{x^2-y^2}$	9.26	1.12	0.63	0.25	0.72	0.31	0.21
				d	8.63	0.92	0.70	0.13	0.61	0.38	0.12
$TaSi_2N_4$	α_1	2.97	Cold-Metal (pn-type)	d_{z^2}	5.36	1.57	–	–	0.39	–	–
				$d_{z^2}+d_{xy}+d_{x^2-y^2}$	9.35	2.14	1.63	0.30	1.03	0.59	0.24
				d	8.58	1.93	1.62	0.24	1.00	0.63	0.21
$TaSi_2P_4$	α_1	3.54	Cold-Metal (p-type)	d_{z^2}	4.31	0.81	–	–	0.29	–	–
				$d_{z^2}+d_{xy}+d_{x^2-y^2}$	8.00	1.12	0.72	0.22	0.75	0.39	0.19
				d	7.60	1.05	0.75	0.18	0.74	0.42	0.16
$TaSi_2As_4$	α_2	3.68	Cold-Metal (p-type)	d_{z^2}	3.90	0.67–		–	0.23	–	–
				$d_{z^2}+d_{xy}+d_{x^2-y^2}$	8.70	1.14	0.68	0.26	0.67	0.36	0.17
				d	7.71	0.86	0.66	0.12	0.60	0.40	0.10
$TaGe_2N_4$	α_1	3.08	SGM (pn-type)	d_{z^2}	5.17	1.42	–	–	0.35	–	–
				$d_{z^2}+d_{xy}+d_{x^2-y^2}$	8.01	1.70	1.28	0.23	0.80	0.45	0.18

Table 2 (continued) | Crystal symmetry, lattice parameter, ground state, correlated subspace, bare Coulomb interaction V, partially screened Hubbard–Kanamori parameters [U, U', J], fully screened counterparts [$\tilde{U}$, $\tilde{U}'$, $\tilde{J}$] (in eV) for d orbitals of TMs in MA_2Z_4 (M=V, Nb, Ta; A=Si, Ge; Z=N, P, As) compounds

MA_2Z_4	Phase	a (Å)	Ground State	Correlated Subspace	V (eV)	U (eV)	U' (eV)	J (eV)	$\tilde{U}$ (eV)	$\tilde{U}'$ (eV)	$\tilde{J}$ (eV)
				d	8.39	1.78	1.45	0.23	0.91	0.54	0.20
$TaGe_2P_4$	α_2	3.61	Cold-Metal (p-type)	d_{z^2}	4.41	0.82	–	–	0.28	–	–
				$d_{z^2}+d_{xy}+d_{x^2-y^2}$	8.30	1.15	0.72	0.22	0.68	0.39	0.15
				d	7.64	1.05	0.74	0.18	0.64	0.43	0.10
$TaGe_2As_4$	α_2	3.77	Cold-Metal (p-type)	d_{z^2}	4.32	0.70	–	–	0.24	–	–
				$d_{z^2}+d_{xy}+d_{x^2-y^2}$	8.56	1.11	0.64	0.24	0.73	0.33	0.20
				d	8.02	1.03	0.68	0.20	0.62	0.40	0.11

Lattice parameters are taken from Ref. 21
SGS spin gapless semiconductor, *SGM* spin gapped metal.

discussed earlier and enables future investigations of correlation effects across the MA_2Z_4 family.

Compared to the 34-valence-electron compounds, the bare Coulomb interactions V in the 33-electron systems are systematically reduced by 1–2 eV. This reduction stems from the smaller nuclear charge of V, Nb, and Ta relative to Cr, Mo, and W, which leads to less contracted atomic orbitals, more spatially extended Wannier functions, and consequently smaller Coulomb interaction parameters. These trends align with prior observations in related materials[18,27,37] and reflect the chemical effects of reduced nuclear charge and orbital delocalization in lighter transition metals.

A similar trend is observed in the partially screened interactions U, U', and J, which decrease from Cr/Mo/W-based compounds to their V/Nb/Ta counterparts. This behavior arises from the combined influence of reduced orbital localization and enhanced screening. For example, in the cold metallic compound α_1-$NbSi_2N_4$, the intra-orbital U is 2.16 eV, while the fully screened $\tilde{U}$ drops to 1.01 eV—less than half of U—owing to strong screening from low-energy $d \rightarrow d$ transitions within the narrow d_{z^2} band crossing the Fermi level.

This pronounced reduction of $\tilde{U}$ relative to U highlights the critical role of low-energy screening channels in metallic systems and motivates a real-space analysis of the distance dependence of Coulomb interactions. To this end, we analyze the spatial decay of $U(r)$ and $\tilde{U}(r)$ in selected 33-valence-electron MA_2Z_4 compounds. For all materials in this class, $U(r)$ is computed up to the sixth nearest neighbor, with the full dataset provided in Table S4 of the Supplementary Information. To illustrate representative screening behavior, Fig. 4e–h shows the real-space profiles of $V(r)$, $U(r)$, and $\tilde{U}(r)$ for the α_1 and β_2 phases of $NbGe_2N_4$ and $TaSi_2N_4$.

In the α_1 phase, both compounds posses a single d_{z^2}-derived band crossing the Fermi level. Accordingly, we restrict the correlated subspace to the d_{z^2} orbital. In this case, the partially screened interaction $U(r)$ remains long-ranged, extending well beyond twelve lattice constants. By contrast, the fully screened $\tilde{U}(r)$ decays more rapidly and becomes negligible after approximately six neighbors, reflecting efficient screening by low-energy metallic states near the Fermi level.

In the β_2 phase, which is metastable but frequently emerges as the second-lowest-energy structure, both $NbGe_2N_4$ and $TaSi_2N_4$ remain metallic, exhibiting n-type cold-metal behavior (see ref. 21 and Table S5 in the Supplementary Information). Unlike the α_1 phase, however, the low-energy states in this configuration involve more entangled orbital characters, necessitating a three-orbital correlated subspace ($d_{z^2} + e_g$) for accurate modeling. Within this subspace, both the partially screened interaction $U(r)$ and the fully screened interaction $\tilde{U}(r)$ decay rapidly with distance, vanishing beyond six lattice spacings (see Fig. 4). This short-range behavior reflects more efficient metallic screening in the β_2 phase. The corresponding real-space Coulomb interaction parameters, both on-site and off-site, are provided in Tables S5 and S6 of the Supplementary Information. These values are particularly relevant for understanding correlation effects in structurally reconstructed β_2 phases, where CDW instabilities are known to emerge.

Table 3 | The on-site (U_{00}^{eff}) and the off-site (U_{01}^{eff}) effective Coulomb interactions are calculated for a specific atomic rearrangement pattern within the β_2 phases of MA_2Z_4 structure, known as the star-of-David configuration

MA_2Z_4	Phase	Correlated Subspace	U_{00}(eV)	U_{01}(eV)
VGe_2N_4	β_2	d_{z^2}	0.17	0.08
		$d_{z^2} + e_g$	1.02	0.63
$NbSi_2N_4$	β_2	d_{z^2}	0.94	0.72
		$d_{z^2} + e_g$	0.54	0.19
$NbGe_2N_4$	β_2	d_{z^2}	0.91	0.65
		$d_{z^2} + e_g$	0.52	0.19
$NbSi_2P_4$	β_2	d_{z^2}	0.16	0.09
		$d_{z^2} + e_g$	0.21	0.09
$TaSi_2N_4$	β_2	d_{z^2}	1.08	0.78
		$d_{z^2} + e_g$	0.61	0.22
$TaGe_2N_4$	β_2	d_{z^2}	0.95	0.68
		$d_{z^2} + e_g$	0.51	0.18
$TaSi_2P_4$	β_2	d_{z^2}	0.16	0.09
		$d_{z^2} + e_g$	0.21	0.09

To connect with these CDW phenomena, we analyze the effective Coulomb interaction parameters relevant for the star-of-David (SOD) reconstruction [see Fig. 1f], which has been theoretically predicted to occur at low temperatures in β_2-phase MA_2Z_4 compounds[21,38]. While our calculations are performed for the undistorted β_2 lattice, they provide critical input for modeling the insulating SOD phase. Using the methodology described in Eq. (9), we extract both the on-site (U_{00}^{eff}) and nearest-neighbor (U_{01}^{eff}) screened Coulomb interactions for several systems with Z = N, as listed in Table 3. We find U_{00}^{eff} values in the range of 0.9–1.1 eV, significantly higher than the 0.65–0.80 eV reported for prototypical CDW systems like NbS_2 and TaS_2[18,39]. In addition, the off-site interaction U_{01}^{eff} reaches up to 75% of the on-site value, indicating strong nonlocal interactions. These features, combined with the narrow bandwidth of the reconstructed SOD phase ($W \approx 0.02$ eV)[38,39], point toward a strong-coupling regime that favors correlation-driven CDW order. The extracted parameters thus form a reliable foundation for future many-body simulations based on extended Hubbard models or methods such as DFT+U and DFT+DMFT. Having established the importance of nonlocal interactions in charge-ordered systems, we now shift our attention to Mn-based MA_2Z_4 compounds, where strong correlations give rise to ferromagnetism and topological phases.

Table 4 | Lattice parameters, electronic ground states, correlated subspaces, and Coulomb interaction parameters for the *d* orbitals of transition-metal atoms in two-dimensional MnA_2Z_4 compounds (A = Bi, Sb; Z = Se, Te) with 41 valence electrons

MA_2Z_4	Phase	a (Å)	Ground State	Correlated Subspace	V (eV)	U (eV)	U' (eV)	J (eV)	$\tilde{U}$ (eV)	$\tilde{U}'$ (eV)	$\tilde{J}$ (eV)
$MnSb_2Se_4$	β_5	3.87	FM-SC	$d_{z^2}+e_g$	12.01	0.45	0.16	0.14	0.27	0.14	0.06
				d	11.52	1.29	0.89	0.26	0.30	0.15	0.08
$MnSb_2Te_4$	β_5	4.23	FM-SC	$d_{z^2}+e_g$	14.16	0.90	0.40	0.23	0.44	0.21	0.11
				d	10.45	1.04	0.70	0.22	0.39	0.22	0.10
$MnBi_2Se_4$	β_5	3.93	FM-SC	$d_{z^2}+e_g$	14.47	0.81	0.39	0.22	0.66	0.52	0.07
				d	12.77	1.67	1.15	0.33	0.73	0.53	0.09
$MnBi_2Te_4$	β_5	4.34	FM-SC	$d_{z^2}+e_g$	14.12	1.07	0.50	0.29	0.29	0.18	0.10
				d	11.56	1.21	0.80	0.26	0.40	0.20	0.10

The listed quantities include the bare intra-orbital Coulomb interaction V, the partially screened Hubbard–Kanamori parameters [U, U', J], and their fully screened counterparts [$\tilde{U}$, $\tilde{U}'$, $\tilde{J}$]. For each compound, values are reported for two distinct correlated subspaces: a three-orbital model ($d_{z^2}+e_g$) and the full d-orbital manifold. Lattice constants are taken from ref. 40,44.
FM-SC ferromagnetic semiconductor.

Coulomb interactions in 41-valence-electron Mn-based topological materials

We now examine the Coulomb interaction parameters in a class of Mn-based MA_2Z_4 compounds with 41 valence electrons, where A = Bi or Sb and Z = Se or Te. These materials, which all crystallize in the β_5 phase, exhibit robust ferromagnetic semiconducting (FM-SC) ground states and are widely recognized for their topologically nontrivial properties[24–26,40–44]. Among them, β_5-$MnBi_2Te_4$ has emerged as a prototypical intrinsic magnetic topological insulator, exhibiting hallmark phenomena such as the quantum anomalous Hall effect, axion electrodynamics, and high-Chern-number states in thin-film form[24,25,41,42]. These magnetic and topological features originate from the interplay between the localized Mn d orbitals and the surrounding Bi/Te p states, motivating a detailed analysis of the effective Coulomb interaction parameters.

To analyze interaction trends in these Mn-based topological compounds, we evaluate the bare Coulomb interaction V, the partially screened Hubbard–Kanamori parameters (U, U', J), and their fully screened counterparts ($\tilde{U}$, $\tilde{U}'$, $\tilde{J}$) for four representative systems: β_5-$MnBi_2Te_4$, β_5-$MnBi_2Se_4$, β_5-$MnSb_2Te_4$, and β_5-$MnSb_2Se_4$. These parameters, obtained from cRPA (RPA) calculations in the non-magnetic reference state, are summarized in Table 4. For each material, we consider two correlated subspaces: a three-orbital model comprising d_{z^2} and e_g orbitals, and the full five-orbital d-manifold.

Several trends emerge from the data in Table 4. Most notably, the bare Coulomb interaction V is consistently larger in the three-orbital subspace, reaching up to 14.5 eV in $MnBi_2Se_4$. This behavior reflects the more localized nature of the d_{z^2} and e_g orbitals that dominate the electronic states near the Fermi level. As shown in Fig. 2e, the remaining two Mn d orbitals lie higher in energy and exhibit significant p-d hybridization, leading to greater spatial delocalization and thus their inclusion in the full five-orbital d-manifold reduces the averaged bare interaction. Upon inclusion of screening, the partially screened U values are substantially reduced, typically falling in the range of 0.45–1.67 eV depending on the compound and subspace. The exchange parameter J ranges from 0.14 to 0.33 eV, indicating moderate intra-atomic exchange interactions that are relevant for stabilizing the ferromagnetic ground state in these materials. To complement these local interaction values, the spatial decay of the partially screened effective U values—extending up to the sixth nearest neighbor—is presented in the Supplementary Information (Table S7), further illustrating the extended nature of Coulomb interactions in the β_5 phase.

Across the series, a clear chemical trend is observed. Substituting Bi with Sb generally lowers both the bare and screened interaction parameters, consistent with the smaller atomic radius and higher electronegativity of Sb. These factors lead to shorter Mn-A bond distances and enhanced hybridization, which in turn increase the overall interaction strength. Similarly, replacing Te with the more localized Se results in slightly larger V values, as expected. The partially screened Hubbard U values for the full d-orbital manifold are consistently larger than those for the three-orbital model. This reflects the fact that, in the full subspace, more screening channels are excluded from the polarization function, leading to reduced screening and hence larger interaction values. In contrast, the three-orbital model retains screening contributions from the remaining d states, resulting in lower U values. The fully screened interactions $\tilde{U}$ and $\tilde{U}'$, though systematically smaller than their partially screened counterparts, remain in the range of 0.27–0.73 eV.

These Coulomb interaction parameters provide a quantitative basis for modeling Mn-based magnetic topological insulators using extended Hubbard models, DFT+DMFT, or DFT+$U(+V)$ approaches. They also offer key insights into how chemical substitution and orbital selection influence the balance between electronic localization and screening, an interplay that underpins the emergence of magnetic and topological phases in this material family.

More broadly, the results for 32-, 33-, 34-, and 41-valence-electron MA_2Z_4 monolayers reveal systematic trends in both the strength and spatial extent of Coulomb interactions. These trends reflect a complex interplay between orbital localization, screening efficiency, and structural phase. For instance, semiconducting 34-valence-electron compounds exhibit relatively strong yet spatially extended interactions, while cold metals in the 33-valence-electron class show sharp contrasts between partially and fully screened interactions, particularly in phases with narrow bands crossing the Fermi level. In metastable β_2 structures, enhanced metallic screening significantly suppresses the long-range components of the interaction. Overall, these findings provide a foundation for describing correlation effects across this material family and offer valuable context for interpreting the collective excitations and magnetic behavior discussed in the subsequent sections.

Correlation strength and magnetic instabilities in MA_2Z_4 materials

To assess the degree of electronic correlations across the MA_2Z_4 family, we evaluate the ratio of the partially screened on-site Coulomb interaction U to the corresponding bandwidth W, commonly denoted as U/W. This dimensionless parameter serves as a key indicator of correlation strength, distinguishing weakly correlated metals from strongly correlated systems, and offers insight into the propensity for magnetic ordering or Mott-like behavior. Typically, systems with $U/W < 1$ are considered weakly correlated, those with $U/W \approx 1$ moderately correlated, and those with $U/W > 1$ strongly correlated. Given the diversity of orbital characters near the Fermi level, we compute U/W for three distinct correlated subspaces: a single-orbital model (typically dominated by the most localized d_{z^2} orbital), a three-orbital model ($d_{z^2}+e_g$), and the full five-orbital d-manifold.

Among the 33-valence-electron compounds, characterized by a half-filled band at the Fermi level, we find large values of the correlation strength U/W. In the single-orbital subspace, U/W frequently exceeds unity. These high ratios reflect narrow bandwidths and reduced metallic screening, resulting from the presence of both internal and external energy gaps around E_F. While the three- and five-orbital subspaces yield lower U/W values due to increased hybridization and broader band dispersions, signatures of strong coupling persist. This trend points to an inherent tendency toward magnetic ordering, consistent with our spin-polarized DFT results and prior theoretical studies.

For the 34-valence-electron Cr-based compounds, we restrict our analysis to the three-orbital and five-orbital correlated subspaces, which more accurately reflect the multiorbital nature of the Cr d-states near the Fermi level. Within these subspaces, the degree of electronic correlation varies significantly with chemical composition. In particular, the nitrogen-based β_2-$CrGe_2N_4$ displays signatures of strong electronic correlation in the three-orbital model, with $U/W = 2.2$, consistent with a narrow bandwidth and reduced screening. This contrasts with the arsenic-based analogue, which exhibits broader bands and enhanced hybridization, leading to more delocalized Cr d-states and weaker correlations. The comparison between N- and As-based systems highlights the role of chemical environment in tuning orbital localization and screening efficiency. These findings indicate that strong correlation effects are primarily confined to the N-based Cr compound, while the As-based system lies in a more moderately correlated regime.

In the case of the 41-valence-electron Mn-based topological compounds, we likewise focus on the three- and five-orbital subspaces to capture the multiorbital character of the Mn-derived states near the Fermi level. Within these subspaces, the correlation strength U/W lies between ~0.6 and 1.7, with slightly reduced values in the five-orbital model due to enhanced hybridization with chalcogen and pnictogen p-orbitals. Although the overall correlation strength remains moderate, the combination of sizable on-site Coulomb repulsion U and finite exchange J is sufficient to stabilize the experimentally observed ferromagnetic semiconducting phases in these compounds[24,25].

Overall, the correlation strength trends across the 33-, 34-, and 41-valence-electron MA_2Z_4 systems reveal a clear evolution governed by orbital localization, electron count, and screening efficiency. The 33-electron materials exhibit strong correlations in narrow half-filled bands, while the 34- and 41-electron systems show more moderate interactions depending on the degree of orbital delocalization. These insights provide a quantitative basis for analyzing magnetic instabilities, which we address next using the Stoner model.

While the correlation strength quantified by U/W provides valuable insight into the electronic interactions in MA_2Z_4 compounds, it does not fully capture the tendency toward magnetic ordering, particularly in metallic systems with a finite density of states at the Fermi level. To complement the U/W analysis, we therefore turn to the Stoner model of itinerant magnetism, which offers a quantitative criterion for the onset of ferromagnetic instability. This framework is especially pertinent for the 33, 34, and 41 valence electron compounds studied here, where magnetism arises from a single transition metal sublattice: V, Nb, or Ta in the 33-valence-electron systems; Cr in the 34-valence-electron systems; and Mn in the 41-valence-electron materials. Our methodology builds on prior work that employed constrained RPA-derived Stoner parameters to analyze spin splitting and magnetic order in half-Heusler compounds with multiple magnetic sublattices[45].

Magnetic instabilities in low-dimensional systems often emerge from a complex interplay between electron-electron interactions, density of states, and the symmetry of the relevant electronic orbitals. In the MA_2Z_4 family, where magnetism originates from a single transition-metal sublattice, these instabilities are generally of itinerant character. For example, our supercell DFT calculations for α_1-VSi_2N_4 reveal a substantial reduction in the V magnetic moment, by nearly 50%—in an antiferromagnetic configuration compared to the ferromagnetic ground state. This pronounced sensitivity of the local moment to the magnetic ordering pattern is a hallmark of itinerant magnetism, in contrast to the localized magnetic moments of Mott systems. To quantitatively assess the tendency toward such itinerant magnetic ordering, we now turn to the Stoner model, which provides a well-defined criterion for the onset of ferromagnetism in metallic systems.

The Stoner criterion states that a system becomes unstable toward ferromagnetism when the product $IN(E_F)$ exceeds unity, where I is the Stoner parameter and $N(E_F)$ is the density of states at the Fermi level in the non-magnetic state. In this work, the Stoner parameter I is obtained from the Slater parameterization of the cRPA Coulomb interaction matrix (see Methods section), using expressions tailored to each correlated subspace: $I = \frac{1}{5}(U_s + 6J_s)$ for the full five-orbital d-manifold, $I = \frac{1}{3}(U_s + 4J_s)$ for the three-orbital model, and $I = U_s$ for the one-orbital case, where Hund's coupling does not contribute. These formulas provide a consistent and physically grounded approach to estimating I from cRPA-derived interaction parameters across different orbital models and materials.

For the 33-valence-electron compounds, magnetic instabilities are most appropriately analyzed using the one-orbital model in all structural phases except the β_2 phase. This choice is supported by the orbital-resolved band structures, which reveal that a single orbital—predominantly d_{z^2}—dominates the electronic states near the Fermi level and contributes most significantly to the magnetic moment, as also reflected in the final column of Table 5. Within this one-orbital subspace, all V-based compounds satisfy the Stoner criterion $IN(E_F) > 1$ and consequently develop magnetic moments close to $1\mu_B$. In contrast, only a few Nb- and Ta-based compounds satisfy the criterion, and even in these cases, the resulting magnetic moments are significantly smaller, typically below $0.5\mu_B$. These reduced magnetic moments are consistent with the smaller exchange splittings observed in spin-polarized DFT calculations (see Fig. S5 in the Supplementary Information). A notable exception is α_1-$TaSi_2N_4$, which satisfies the Stoner criterion with $IN(E_F) = 1.37$ in the one-orbital model, yet remains nonmagnetic in spin-polarized DFT. This discrepancy underscores a limitation of the Stoner model when used with cRPA-derived interaction parameters. Specifically, the Stoner expressions employed here are derived from the Hartree–Fock solution of the multiorbital Hubbard model[46] and neglect dynamic correlation effects, which are known to reduce the Stoner parameter by up to 40%. Such correlations may shift the actual Stoner product below the critical threshold, thereby explaining the absence of magnetism in α_1-$TaSi_2N_4$.

For the β_2-phase structures of the 33-valence-electron compounds, the one-orbital model becomes inadequate due to the broader distribution of electronic states near the Fermi level. Instead, the three-orbital model provides a more accurate representation of the relevant correlated subspace. Within this model, none of the Nb- and Ta-based β_2-phase compounds satisfy the Stoner criterion, consistent with their paramagnetic ground states observed in spin-polarized DFT calculations. In contrast, β_2-VGe_2N_4 emerges as the only V-based compound in the β_2 phase that fulfills the Stoner criterion in the three-orbital model, while failing to do so in the one-orbital case. This behavior highlights the spatially extended nature of the magnetic orbitals and underscores the necessity of an enlarged correlated subspace for an accurate description of magnetic tendencies in this system.

Turning to the 34- and 41-valence-electron compounds, the three-orbital subspace provides the most appropriate description of magnetism, as the correlated states near the Fermi level involve multiple orbitals beyond the d_{z^2} component. For this reason, we do not report one-orbital results for both the Cr- and Mn-based compounds. As shown in Table 5, all Cr- and Mn-based systems satisfy the Stoner criterion $IN(E_F) > 1$ in the three-orbital model, indicating a strong tendency toward ferromagnetic ordering. The Mn-based layered topological compounds exhibit particularly large $IN(E_F)$ values exceeding 2, along with magnetic moments above $3\mu_B$, consistent with their well-established ferromagnetic semiconducting character. The three Cr-based compounds, β_2-$CrGe_2N_4$, β_1-$CrSi_2As_4$, and β_1-$CrGe_2As_4$, exhibit Stoner instabilities with $IN(E_F) > 1$ and develop sizable magnetic moments in spin-polarized DFT calculations. These findings confirm the reliability of the Stoner model in predicting itinerant ferromagnetism in

Table 5 | Valence electron count (VEC), correlation strength *U/W*, Stoner parameter *I* (in eV), non-magnetic density of states at the Fermi level $N(E_F)$ (in states/eV), Stoner criterion $IN(E_F)$, and spin-polarized magnetic moment *m* (in μ_B) for selected MA_2Z_4 compounds with 33, 34, and 41 valence electrons

		1-orbital subspace				3-orbital subspace				5-orbital subspace				
MA_2Z_4	VEC	*U/W*	*I*	$N(E_F)$	$I.N(E_F)$	*U/W*	*I*	$N(E_F)$	$I.N(E_F)$	*U/W*	*I*	$N(E_F)$	$I.N(E_F)$	m_M
α_1-VSi_2N_4	33	1.37	1.48	1.31	1.94	0.80	1.50	2.53	3.80	0.54	0.97	2.53	2.45	1.03
δ_4-VSi_2P_4	33	1.14	0.80	1.42	1.14	0.48	0.95	2.67	2.54	0.38	0.61	2.67	1.63	1.06
α_2-VSi_2As_4	33	1.03	0.73	1.66	1.21	0.48	0.94	3.27	3.07	0.38	0.60	3.27	1.96	1.06
β_2-VGe_2N_4	33	0.54	0.43	1.40	0.60	1.62	1.38	2.15	2.97	0.57	0.90	3.06	2.75	1.12
α_2-VGe_2P_4	33	0.88	0.78	1.37	1.07	0.47	0.98	2.75	2.70	0.38	0.63	2.75	1.73	0.79
α_2-VGe_2As_4	33	0.86	0.66	1.62	1.07	0.50	0.94	3.29	3.09	0.37	0.60	3.29	1.97	1.06
α_1-$NbSi_2N_4$	33	1.24	1.51	1.03	1.56	0.39	1.14	1.90	2.17	0.33	0.76	1.90	1.44	0.43
α_1-$NbSi_2P_4$	33	0.60	0.71	1.03	0.73	0.36	0.68	1.73	1.18	0.29	0.46	1.73	0.80	–
α_2-$NbSi_2As_4$	33	0.62	0.63	1.17	0.74	0.39	0.74	2.11	1.56	0.27	0.43	2.11	0.91	–
α_1-$NbGe_2N_4$	33	1.28	1.38	1.25	1.73	0.44	1.04	2.37	2.46	0.28	0.62	2.37	1.47	0.63
α_2-$NbGe_2P_4$	33	0.63	0.72	1.06	0.76	0.37	0.71	1.87	1.33	0.28	0.48	1.87	0.90	–
α_2-$NbGe_2As_4$	33	0.60	0.61	1.16	0.70	0.38	0.70	2.05	1.44	0.27	0.35	2.05	0.72	–
α_1-$TaSi_2N_4$	33	1.12	1.57	0.87	1.37	0.35	1.12	1.65	1.85	0.30	0.71	1.65	1.17	–
α_1-$TaSi_2P_4$	33	0.56	0.81	0.97	0.79	0.33	0.67	1.63	1.09	0.27	0.44	1.63	0.72	–
α_2-$TaSi_2As_4$	33	0.55	0.67	1.10	0.74	0.37	0.73	1.91	1.39	0.24	0.33	1.91	0.63	–
α_1-$TaGe_2N_4$	33	1.26	1.42	1.05	1.49	0.37	0.87	2.07	1.80	0.31	0.66	2.07	1.37	0.37
α_2-$TaGe_2P_4$	33	0.57	0.82	0.97	0.80	0.33	0.67	1.70	1.14	0.27	0.44	1.70	0.75	–
α_2-$TaGe_2As_4$	33	0.55	0.70	1.07	0.75	0.35	0.68	1.86	1.26	0.28	0.46	1.86	0.86	–
β_2-$NbSi_2N_4$	33	0.39	1.20	0.36	0.43	0.39	1.05	0.61	0.64	0.30	0.72	0.77	0.55	–
β_2-$NbSi_2P_4$	33	0.15	0.25	0.80	0.20	0.29	0.49	1.31	0.64	0.25	0.31	1.75	0.54	–
β_2-$NbGe_2N_4$	33	0.53	1.17	0.48	0.56	0.50	0.99	0.75	0.74	0.29	0.62	0.98	0.61	–
β_2-$TaSi_2N_4$	33	0.40	1.36	0.28	0.38	0.38	1.13	0.49	0.55	0.29	0.68	0.62	0.42	–
β_2-$TaSi_2P_4$	33	0.14	0.26	0.74	0.19	0.24	0.48	1.14	0.55	0.22	0.35	1.49	0.52	–
β_2-$TaGe_2N_4$	33	0.47	1.21	0.36	0.44	0.40	0.94	0.58	0.55	0.29	0.67	0.75	0.50	–
β_1-$CrSi_2As_4$	34	–	–	–	–	0.53	0.75	2.28	1.71	0.33	0.54	2.63	1.42	2.80
β_2-$CrGe_2N_4$	34	–	–	–	–	2.22	1.64	1.84	3.02	0.74	1.08	2.37	2.56	2.32
β_1-$CrGe_2As_4$	34	–	–	–	–	0.23	0.32	3.93	1.26	0.17	0.21	4.50	0.95	2.88
β_5-$MnSb_2Se_4$	41	–	–	–	–	0.56	0.33	6.50	2.15	0.59	0.60	7.90	4.74	3.38
β_5-$MnSb_2Te_4$	41	–	–	–	–	1.41	0.59	4.09	2.41	0.80	0.50	5.10	2.55	4.21
β_5-$MnBi_2Se_4$	41	–	–	–	–	1.21	0.56	6.30	3.53	1.00	0.77	7.87	6.06	3.52
β_5-$MnBi_2Te_4$	41	–	–	–	–	1.73	0.73	3.76	2.74	1.03	0.58	4.73	2.74	4.27

Values are reported for three correlated subspaces: the single-orbital model (predominantly d_{z^2}), the three-orbital model ($d_{z^2} + e_g$), and the full five-orbital *d*-manifold. The table enables a comparative assessment of correlation strength and the tendency toward ferromagnetic ordering, as indicated by the Stoner criterion $IN(E_F) > 1$, and includes the resulting magnetic moments from spin-polarized DFT calculations.

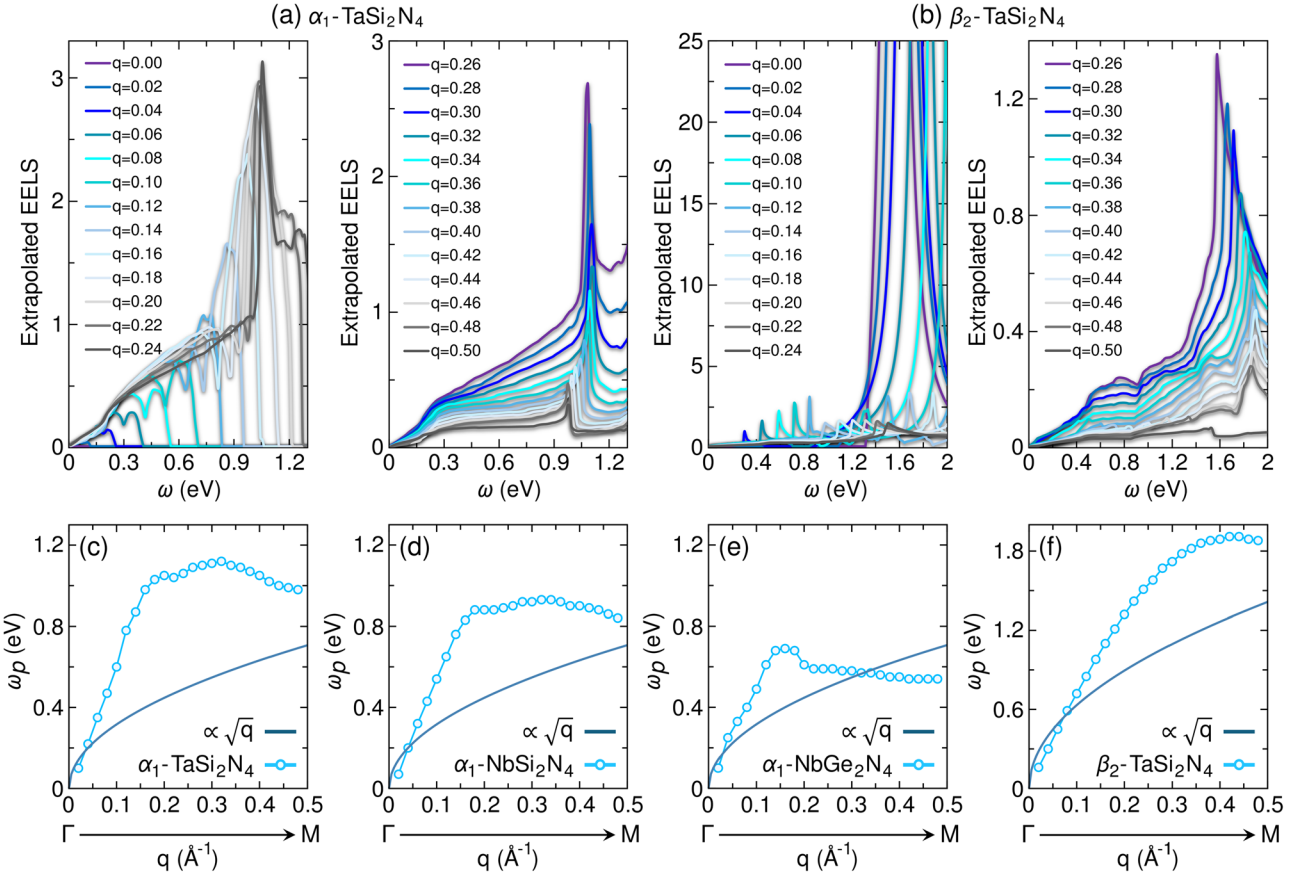

Fig. 5 | Plasmonic properties of selected 33-valence-electron MA_2Z_4 cold metallic compounds. The calculated electron energy loss spectra $L(\mathbf{q}, \omega)$ for wavevectors along the Γ--M direction in (**a**) α_1-$TaSi_2N_4$ and (**b**) β_2-$TaSi_2N_4$. Plasmon dispersion relations extracted from the peak positions in $L(\mathbf{q}, \omega)$ are plotted in (**c**)–(**f**) for four representative materials: **c** α_1-$TaSi_2N_4$, **d** α_1-$NbSi_2N_4$, **e** α_1-$NbGe_2N_4$, and **f** β_2-$TaSi_2N_4$. The results show pronounced deviations from conventional $\sqrt{q}$ plasmon dispersion, including linear and negative-slope regimes characteristic of cold-metal band structures.

Cr- and Mn-based MA_2Z_4 systems and emphasize the role of multi-orbital correlations in stabilizing their magnetic ground states.

In summary, the Stoner model analysis across the MA_2Z_4 family highlights the crucial role of both electron count and orbital character in governing magnetic instabilities. For 33-valence-electron compounds, the magnetism is predominantly driven by a single localized orbital, whereas in the 34- and 41-electron systems, multi-orbital effects and enhanced density of states at the Fermi level lead to robust ferromagnetic tendencies. The agreement between Stoner criterion predictions and spin-polarized DFT results is generally strong, but deviations, such as in α_1-$TaSi_2N_4$, reveal the limitations of the Hartree–Fock-based approach when many-body correlation effects are significant. Despite these limitations, the combined U/W and Stoner analyses offer a comprehensive framework for understanding the correlation-driven magnetism in this diverse materials family, laying the foundation for subsequent exploration of their collective spin excitations.

Plasmon dispersion in cold metallic compounds

Plasmons—collective oscillations of the electron density, play a central role in governing the optical and charge-response properties of low-dimensional systems. In two-dimensional materials, they exhibit strong spatial confinement, electrostatic tunability, and enhanced near-field intensities, making them promising candidates for applications in photodetectors, sensors, modulators, and energy-harvesting technologies[47,48]. However, the practical realization of such plasmonic devices is often hindered by dissipative losses due to Landau damping, phonon coupling, or disorder-induced scattering. A key strategy to suppress these losses is to eliminate low-energy electron-hole pair excitations. This condition can be naturally fulfilled in systems with a narrow metallic band energetically isolated by internal and external gaps, as recently observed in a class of 2D cold metals.

Motivated by recent observations, particularly the emergence of low-loss plasmons in cold metallic TMDs such as TaS_2, $TaSe_2$, and $NbSe_2$[10,49,50], we turn our attention to structurally related MA_2Z_4 monolayers with 33 valence electrons. We focus on four representative compounds: α_1-$TaSi_2N_4$, α_1-$NbSi_2N_4$, α_1-$NbGe_2N_4$, and β_2-$TaSi_2N_4$, which exhibit either pn-type or n-type cold metallic behavior. The Nb-based systems, while exhibiting small exchange splittings in their magnetic ground states (see Fig. S5 in the Supplementary Information), are treated in the non-magnetic configuration to isolate plasmonic features arising from their band topology. All four compounds feature a narrow d_{z^2}-derived band crossing the Fermi level; in the three α_1-phase pn-type cold metals, this band is flanked by well-defined energy gaps above and below E_F, whereas in the β_2-phase $TaSi_2N_4$, only the lower gap is present, characteristic of an n-type cold metal. This band topology suppresses interband transitions and Landau damping, making these systems ideal candidates for supporting low-loss, unconventional plasmon modes.

To evaluate the plasmonic response and characterize the collective charge excitations in these systems, we compute the loss function $L(\mathbf{q}, \omega) = -\mathrm{Im}[1/\epsilon_m(\mathbf{q}, \omega)]$, where $\epsilon_m(\mathbf{q}, \omega) = 1/\epsilon_{00}^{-1}(\mathbf{q}, \omega)$ denotes the macroscopic dielectric function. Plasmon modes appear as peaks in $L(\mathbf{q}, \omega)$, and their dispersion is extracted by tracking the peak positions as a function of in-plane wavevector $q = |\mathbf{q}|$. Figure 5a and b shows representative loss spectra, while 5c–f display the resulting dispersion relations. While three-dimensional metals exhibit finite plasmon energies at $q = 0$ and conventional 2D metals follow $\omega_p \propto \sqrt{q}$ behavior, the MA_2Z_4 cold metals show markedly different trends.

In particular, the α_1-phase compounds exhibit a distinct plasmon dispersion featuring a nearly linear slope at small q, followed by an extended flat region, and ultimately a negative slope at larger momenta. This non-monotonic behavior is strongly suppressed in the β_2 phase. The underlying mechanism can be traced to the pn-type cold metallic band structure (see Fig. S4 in the Supplementary Information): a narrow d_{z^2}-derived band crossing the Fermi level is energetically isolated by internal and external gaps, which limit the phase space for electron-hole pair excitations and suppress interband transitions near the plasmon energy. As demonstrated in recent electron energy-loss spectroscopy studies of 2H-TMDs such as 1H-TaS_2, 1H-$TaSe_2$, and 1H-$NbSe_2$[49], the flattening and eventual downturn of the plasmon dispersion result from a progressive weakening of the screening response at finite momentum. In that context, the initial plasmon dispersion is positive due to effective low-energy screening; however, as q increases, interband transitions are no longer available to efficiently screen the plasmon, leading first to a plateau and then to a decrease in plasmon energy. This mechanism closely parallels the behavior observed in our pn-type MA_2Z_4 compounds. The β_2-phase $TaSi_2N_4$, by contrast, lacks the upper gap and exhibits conventional n-type behavior, resulting in a more monotonic dispersion. Our findings thus position MA_2Z_4 cold metals as promising platforms for low-loss 2D plasmonics, where dispersion characteristics can be engineered through band-structure design and phase control.

We note, however, that the plasmon dispersions presented here are derived from DFT-based band structures, which are known to underestimate band gaps relative to many-body approaches such as the GW method. In our recent GW study of 2D cold metallic TMDs and 33-valence-electron MA_2Z_4 compounds[51], we showed that both internal and external gaps are significantly enhanced compared to their DFT counterparts. As the plasmon behavior in cold metals is strongly tied to the energetic separation between the narrow metallic band and surrounding states, larger GW gaps would further reduce interband screening channels and likely enhance the flattening or downturn of the dispersion. These considerations suggest that the unconventional plasmon features reported here may be even more pronounced when many-body corrections are taken into account.

While our analysis has focused on four representative compounds—α_1-$TaSi_2N_4$, α_1-$NbSi_2N_4$, α_1-$NbGe_2N_4$, and β_2-$TaSi_2N_4$—several other 33-valence-electron MA_2Z_4 monolayers listed in Table 2 exhibit similar electronic features. Notable examples include α_1-$TaGe_2N_4$, β_2-VGe_2N_4, and α_2-VGe_2P_4, all of which possess narrow d_{z^2} bands crossing E_F and display pn-type cold metallic character. Their similarly restricted interband phase space suggests they may also support low-loss plasmon modes with linear and negative dispersion regimes. A broader theoretical and experimental exploration of these systems could open new avenues for designing tunable 2D plasmonic materials based on pn-type cold metals.

Overall, our results provide a comprehensive mapping of effective Coulomb interactions and their implications across semiconducting, metallic, cold-metallic, magnetic, and topological MA_2Z_4 monolayers. Using cRPA, we computed material-specific interaction parameters and revealed unconventional screening behavior in both semiconductors and cold-metallic systems. Our analysis points to the emergence of strong-coupling tendencies in several 33- and 34-valence-electron compounds, including signatures of proximity to Mott or CDW instabilities in narrow-band phases. In addition, we identified magnetic instabilities in V-, Nb-, Cr-, and Mn-based monolayers through a subspace-resolved Stoner criterion. Finally, our exploration of a selected set of cold-metallic compounds uncovered anomalous plasmon dispersions characterized by nearly non-dispersive low-energy modes. These findings position MA_2Z_4 monolayers as a fertile platform for investigating screening, correlation-driven instabilities, and low-energy collective behavior in two dimensions.

Methods

Computational details

Our first-principles calculations are based on DFT within the full-potential linearized augmented plane wave framework, as implemented in the FLEUR code[52]. The exchange-correlation functional is treated using the generalized gradient approximation in the Perdew–Burke–Ernzerhof (PBE) parameterization[53]. We perform both non-spin-polarized and spin-polarized DFT calculations where appropriate: non-magnetic calculations are used for all cRPA evaluations, while spin-polarized calculations are carried out only for compounds investigated using the Stoner model of magnetic instability. All calculations are based on experimentally reported or previously published lattice structures and atomic positions, without any additional structural relaxation[21,40,44].

For the self-consistent DFT calculations, we use a $16 \times 16 \times 1$ **k**-point mesh in the 2D Brillouin zone and a plane-wave cutoff of $G_{\max} = 4.5\,\mathrm{bohr}^{-1}$ for the interstitial wavefunctions. Wannier projectors are constructed for the transition metal d orbitals using the WANNIER90 package[54], interfaced with FLEUR code. The number and character of the Wannier functions are adapted to the orbital content near the Fermi level in each system, with particular attention to one-, three-, and five-orbital correlated subspaces.

The outputs of the DFT calculations serve as input for the SPEX code[55–57], which we use to evaluate the partially screened and fully screened Coulomb interaction matrices within the cRPA and the full RPA. For these calculations, we employ a $12 \times 12 \times 1$ **k**-point grid and include sufficient unoccupied states to ensure convergence of the polarization function and dielectric screening.

Overview of the cRPA formalism

The cRPA provides an ab initio framework for computing the effective Coulomb interaction among localized electrons, while systematically excluding screening processes arising within the correlated subspace[11,13,58,59]. This method yields frequency-dependent matrix elements of the partially screened interaction $U(\omega)$, including on-site, interorbital, exchange, and long-range components.

In the cRPA formalism, the total polarization function P is decomposed into two parts: $P = P_d + P_r$, where P_d includes only transitions within the correlated subspace, and P_r accounts for the remaining screening channels. The partially screened Coulomb interaction is then obtained as:

$$U(\omega) = \left[1 - vP_r(\omega)\right]^{-1} v, \tag{1}$$

where v is the bare Coulomb interaction. The fully screened interaction $\tilde{U}(\omega)$ is subsequently obtained by applying the residual screening from the correlated subspace:

$$\tilde{U}(\omega) = \left[1 - U(\omega)P_d(\omega)\right]^{-1} U(\omega). \tag{2}$$

The static matrix elements U are evaluated in the basis of MLWFs $w_{in}(\mathbf{r})$ as:

$$\begin{aligned} U_{in_1,jn_3;in_2,jn_4} = \int d\mathbf{r} \int d\mathbf{r}'\, w^*_{in_1}(\mathbf{r})\, w^*_{jn_3}(\mathbf{r}') \\ \times U(\mathbf{r},\mathbf{r}',\omega=0)\, w_{jn_4}(\mathbf{r}')\, w_{in_2}(\mathbf{r}). \end{aligned} \tag{3}$$

In this work, we consider three distinct correlated subspaces: a one-orbital model (typically dominated by a localized d_{z^2}-like orbital), a three-orbital model, and the full five-orbital d-manifold. To characterize the effective interaction strength in these subspaces, we extract average Coulomb parameters using two standard parameterizations. For most of the analysis in this work, including the determination of correlation strength via U/W, we adopt the Hubbard–Kanamori parametrization, which provides intraorbital (U), interorbital (U'), and exchange (J) interactions defined by:

$$U = \frac{1}{L}\sum_m U_{mm;mm}, \tag{4}$$

$$U' = \frac{1}{L(L-1)}\sum_{m\neq n} U_{mn;mn}, \tag{5}$$

$$J = \frac{1}{L(L-1)} \sum_{m \neq n} U_{mn;nm}, \tag{6}$$

where L = 1, 3, or 5 denotes the number of correlated orbitals in the subspace. These expressions are used to extract orbital-averaged interactions consistent with multiorbital Hubbard or Kanamori-type Hamiltonians. In addition to the partially screened parameters discussed above, one can also define the corresponding fully screened ($\tilde{U}$, $\tilde{U}'$, $\tilde{J}$) and bare (V, V', J_V) Coulomb parameters using the same averaging scheme. The fully screened interaction $\tilde{U}$ includes all screening channels, while the bare interaction V is calculated from the unscreened Coulomb kernel and reflects the spatial extent and localization of the Wannier orbitals. Together, these different levels of screening provide a comprehensive picture of the interaction landscape and its material dependence.

In addition, to calculate the Stoner parameter I, we use the Slater parametrization of the Coulomb matrix. This orbital-averaged form simplifies the interaction to number-operator terms and is given by:

$$U_S = \frac{1}{L^2} \sum_{m,n} U_{mn;mn}, \tag{7}$$

$$J_S = U_S - \frac{1}{L(L-1)} \sum_{m \neq n} \left(U_{mn;mn} - U_{mn;nm} \right). \tag{8}$$

This parametrization ensures consistency with mean-field models of itinerant magnetism and enables a subspace-resolved evaluation of magnetic instabilities.

Together, the Hubbard–Kanamori and Slater parameterizations provide a consistent framework for quantifying electron correlation strength, analyzing orbital-dependent interactions, and identifying the onset of magnetic tendencies across the chemically and electronically diverse MA_2Z_4 monolayers.

Calculating Coulomb interaction parameters for the various structural phases of MA_2Z_4 monolayers is computationally feasible. However, in CDW phases with SOD reconstructions, the unit cell expands significantly, comprising 91 atoms, including 13 transition metal (TM) sites. Direct cRPA calculations for these large supercells are prohibitively expensive. To estimate the effective on-site interaction in such systems, we average the long-range interaction over all TM-TM site pairs within a single star cluster of the corresponding undistorted β structure:

$$U^{\text{eff}} = \frac{1}{13^2} \sum_{\mathbf{R},\mathbf{R}'} U_{\mathbf{R}-\mathbf{R}'}, \tag{9}$$

where $\mathbf{R}$ and $\mathbf{R}'$ label the positions of TM atoms within the star. This average defines the effective on-site interaction U_{00}^{eff} for that star[39,60].

To estimate the effective intersite interaction U_{01}^{eff} between neighboring stars in the reconstructed CDW lattice, one instead averages over all TM site pairs where $\mathbf{R}$ belongs to star A and $\mathbf{R}'$ belongs to the nearest-neighboring star B (see Fig. 1(f) for a schematic of the SOD geometry). This approximation captures the key interaction scales relevant for describing electronic correlations in the SOD phase.

Data availability

All data generated in this study are provided in the main text and Supplementary Information of this article. No additional datasets were generated or analyzed.

Received: 7 August 2025; Accepted: 2 October 2025;
Published online: 18 November 2025

References

1. Novoselov, K. S. et al. Two-dimensional gas of massless Dirac fermions in graphene. *Nature* **438**, 197–200 (2005).
2. Manzeli, S., Ovchinnikov, D., Pasquier, D., Yazyev, O. V. & Kis, A. 2d transition metal dichalcogenides. *Nat. Rev. Mater.* **2**, 1–15 (2017).
3. Wang, L. et al. Correlated electronic phases in twisted bilayer transition metal dichalcogenides. *Nat. Mater.* **19**, 861–866 (2020).
4. Broholm, C. et al. Quantum spin liquids. *Science* **367**, eaay0668 (2020).
5. Cao, Y. et al. Unconventional superconductivity in magic-angle graphene superlattices. *Nature* **556**, 43–50 (2018).
6. Cudazzo, P., Tokatly, I. V. & Rubio, A. Dielectric screening in two-dimensional insulators: Implications for excitonic and impurity states in graphane. *Phys. Rev. B* **84**, 085406 (2011).
7. Andersen, K., Latini, S. & Thygesen, K. Dielectric genome of van der Waals heterostructures. *Nano Lett.* **15**, 4616–4621 (2015).
8. Steinke, C., Wehling, T. O. & Rösner, M. Coulomb-engineered heterojunctions and dynamical screening in transition metal dichalcogenide monolayers. *Phys. Rev. B* **102**, 115111 (2020).
9. Ugeda, M. M. et al. Giant bandgap renormalization and excitonic effects in a monolayer transition metal dichalcogenide semiconductor. *Nat. Mater.* **13**, 1091–1095 (2014).
10. da Jornada, F. H., Xian, L., Rubio, A. & Louie, S. G. Universal slow plasmons and giant field enhancement in atomically thin quasi-two-dimensional metals. *Nat. Commun.* **11**, 1013 (2020).
11. Aryasetiawan, F. et al. Frequency-dependent local interactions and low-energy effective models from electronic structure calculations. *Phys. Rev. B* **70**, 195104 (2004).
12. Miyake, T. & Aryasetiawan, F. Screened Coulomb interaction in the maximally localized Wannier basis. *Phys. Rev. B* **77**, 085122 (2008).
13. Şaşıoğlu, E., Friedrich, C. & Blügel, S. Effective coulomb interaction in transition metals from constrained random-phase approximation. *Phys. Rev. B Condens. Matter Mater. Phys.* **83**, 121101 (2011).
14. Van Loon, E. G., Rösner, M., Katsnelson, M. I. & Wehling, T. O. Random phase approximation for gapped systems: Role of vertex corrections and applicability of the constrained random phase approximation. *Phys. Rev. B* **104**, 045134 (2021).
15. Cunningham, B., Grüning, M., Pashov, D. & Van Schilfgaarde, M. QS*GW*: Quasiparticle self-consistent *GW* with ladder diagrams in *W*. *Phys. Rev. B* **108**, 165104 (2023).
16. Zhang, G., Hadipour, H. & Pavarini, E. Nature of the high-pressure insulating state in Sr_2IrO_4: Mott picture. *Phys. Rev. B* **111**, L121101 (2025).
17. Yue, C. et al. Correlated electronic structures and unconventional superconductivity in bilayer nickelate heterostructures. *Natl. Sci. Rev.* **12**, nwaf253 (2025).
18. Ramezani, H. R. et al. Nonconventional screening of Coulomb interaction in two-dimensional semiconductors and metals: A comprehensive constrained random phase approximation study of MX_2 (M = Mo, W, Nb, Ta; X = S, Se, Te). *Phys. Rev. B* **109**, 125108 (2024).
19. Acharya, S. et al. Importance of charge self-consistency in first-principles description of strongly correlated systems. *npj Comput. Mater.* **7**, 208 (2021).
20. Hong, Y. et al. Chemical vapor deposition of layered two-dimensional $MoSi_2N_4$ materials. *Science* **369**, 670–674 (2020).
21. Wang, L. et al. Intercalated architecture of MA_2Z_4 family layered van der waals materials with emerging topological, magnetic and superconducting properties. *Nat. Commun.* **12**, 2361 (2021).
22. Latychevskaia, T., Bandurin, D. A. & Novoselov, K. S. $MoSi_2N_4$-like crystals–the new family of two-dimensional materials. *Nat. Rev. Phys.* **6**, 426–438 (2024).
23. Tho, C. C. et al. MA_2Z_4 family heterostructures: promises and prospects. *Appl. Phys. Rev.* **10**, 041307 (2023).
24. Guo, H. et al. Controllable synthesis of high-quality magnetic topological insulator $MnBi_2Te_4$ and $MnBi_4Te_7$ multilayers by chemical vapor deposition. *Nano Lett.* **24**, 15788–15795 (2024).
25. Otrokov, M. M. et al. Prediction and observation of an antiferromagnetic topological insulator. *Nature* **576**, 416–422 (2019).

26. Gao, A. et al. An antiferromagnetic diode effect in even-layered $MnBi_2Te_4$. *Nat. Electron.* **7**, 751–759 (2024).
27. Yekta, Y. et al. Strength of effective coulomb interaction in two-dimensional transition-metal halides MX_2 and MX_3 (M = Ti, V, Cr, Mn, Fe, Co, Ni; X = Cl, Br, I). *Phys. Rev. Mater.* **5**, 034001 (2021).
28. Wozniak, T., e hani, U., Junior, P. E. F., Ramzan, M. S. & Kuc, A. B. Electronic and excitonic properties of MSi_2Z_4 monolayers. *Small* **19**, 2206444 (2023).
29. Sun, M., Fiorentin, M. R., Schwingenschlögl, U. & Palummo, M. Excitons and light-emission in semiconducting $MoSi_2X_4$ two-dimensional materials. *npj 2D Mater. Appl.* **6**, 81 (2022).
30. Campo, V. L. Jr. & Cococcioni, M. Extended DFT+U+V method with on-site and inter-site electronic interactions. *J. Phys. Condens. Matter.* **22**, 055602 (2010).
31. Timrov, I., Marzari, N. & Cococcioni, M. Self-consistent Hubbard parameters from density-functional perturbation theory in the ultrasoft and projector-augmented wave formulations. *Phys. Rev. B* **103**, 045141 (2021).
32. Wang, X. L. Proposal for a new class of materials: Spin gapless semiconductors. *Phys. Rev. Lett.* **100**, 156404 (2008).
33. Şaşıoğlu, E. et al. Spin gapped metals: A novel class of materials for multifunctional spintronic devices. *J. Magn. Magn. Mater.* **615**, 172792 (2025).
34. Zhang, L. & Liu, F. High-throughput approach to explore cold metals for electronic and thermoelectric devices. *npj Comput. Mater.* **10**, 78 (2024).
35. Feng, Y., Wang, Z., Zuo, X. & Gao, G. Electronic phase transition, spin filtering effect, and spin seebeck effect in 2d high-spin-polarized VSi_2X_4 (X = N, P, As). *Appl. Phys. Lett.* **120**, 092405 (2022).
36. Feng, X. et al. Valley-related multiple hall effect in monolayer VSi_2P_4. *Phys. Rev. B* **104**, 075421 (2021).
37. Aghaee, A. K., Belbasi, S. & Hadipour, H. Ab initio calculation of the effective coulomb interactions in MX_2 (M = Ti, V, Cr, Mn, Fe, Co, Ni; X = S, Se, Te): intrinsic magnetic ordering and Mott phase. *Phys. Rev. B* **105**, 115115 (2022).
38. Wang, L. et al. Intercalating architecture for the design of charge density wave in metallic MA_2Z_4 materials. *Nano Lett*. **24**, 11279–11285 (2024).
39. Kim, T. J., Jeong, M. Y. & Han, M. J. First principles investigation of screened Coulomb interaction and electronic structure of low-temperature phase TaS_2. *iScience* **26**, 106681 (2023).
40. Zhu, T. et al. Synthesis, magnetic properties, and electronic structure of magnetic topological insulator $MnBi_2Se_4$. *Nano Lett*. **21**, 5083–5090 (2021).
41. Qiu, J.-X. et al. Observation of the axion quasiparticle in 2d $MnBi_2Te_4$. *Nature* **641**, 62–69 (2025).
42. Vyazovskaya, A. Y., Bosnar, M., Chulkov, E. V. & Otrokov, M. M. Intrinsic magnetic topological insulators of the $MnBi_2Te_4$ family. *Commun. Mater.* **6**, 88 (2025).
43. Zhang, E. et al. Observation of edge supercurrent in topological antiferromagnet $MnBi_2Te_4$-based Josephson junctions. *Sci. Adv.* **11**, eads8730 (2025).
44. Wimmer, S. et al. Mn-rich $MnSb_2Te_4$: a topological insulator with magnetic gap closing at high Curie temperatures of 45–50 k. *Adv. Mater.* **33**, 2102935 (2021).
45. Şaşıoğlu, E. et al. Itinerant versus localized magnetism in spin gapped metallic half-heusler compounds: Stoner criterion and magnetic interactions. Preprint at https://arxiv.org/abs/2506.03416 (2025).
46. Stollhoff, G., Oleś, A. M. & Heine, V. Stoner exchange interaction in transition metals. *Phys. Rev. B* **41**, 7028–7041 (1990).
47. Grigorenko, A., Polini, M. & Novoselov, K. Graphene plasmonics. *Nat. Photonics* **6**, 749–758 (2012).
48. Low, T. et al. Polaritons in layered two-dimensional materials. *Nat. Mater.* **16**, 182–194 (2017).
49. van Wezel, J. et al. Effect of charge order on the plasmon dispersion in transition-metal dichalcogenides. *Phys. Rev. Lett.* **107**, 176404 (2011).
50. Gjerding, M. N., Pandey, M. & Thygesen, K. S. Band structure engineered layered metals for low-loss plasmonics. *Nat. Commun.* **8**, 15133 (2017).
51. Beida, W. et al. Correlation effects in two-dimensional MX_2 and MA_2Z_4 (M = Nb, Ta; X = S, Se, Te; A= Si, Ge; Z = N, P) cold metals: Implications for device applications. *Phys. Rev. Mater.* **9**, 014006 (2025).
52. Wortmann, D. et al. FLEUR. *Zenodo* https://doi.org/10.5281/zenodo.7576163 (2023).
53. Perdew, J. P., Burke, K. & Ernzerhof, M. Generalized gradient approximation made simple. *Phys. Rev. Lett.* **77**, 3865 (1996).
54. Marzari, N. & Vanderbilt, D. Maximally localized generalized Wannier functions for composite energy bands. *Phys. Rev. B* **56**, 12847 (1997).
55. Friedrich, C., Blügel, S. & Schindlmayr, A. Efficient implementation of the *GW* approximation within the all-electron FLAPW method. *Phys. Rev. B Condens. Matter Mater. Phys.* **81**, 125102 (2010).
56. Schindlmayr, A., Friedrich, C., Şaşıoğlu, E. & Blügel, S. First-principles calculation of electronic excitations in solids with Spex. *Z. f.ür. Physikalische Chem.* **224**, 357–368 (2010).
57. Friedrich, C. et al. Spex code https://doi.org/10.5281/zenodo.14017762 (2024).
58. Nomura, Y. et al. Effective on-site interaction for dynamical mean-field theory. *Phys. Rev. B* **86**, 085117 (2012).
59. Vaugier, L., Jiang, H. & Biermann, S. Hubbard U and Hund exchange J in transition metal oxides: screening versus localization trends from constrained random phase approximation. *Phys. Rev. B* **86**, 165105 (2012).
60. Kamil, E. et al. Electronic structure of single layer 1T-$NbSe_2$: interplay of lattice distortions, non-local exchange, and Mott-Hubbard correlations. *J. Phys. Condens. Matter.* **30**, 325601 (2018).

Acknowledgements

This work was supported by the Iran National Science Foundation (INSF) under Project No. 4044100, the Collaborative Research Center CRC/TRR 227 of the Deutsche Forschungsgemeinschaft (DFG), and the European Union (EFRE) via Grant No. ZS/2016/06/79307.

Author contributions

S.L. and I.M. conceived and guided the project. H.H. and E.Ş. coordinated the DFT and cRPA calculations and wrote the manuscript. F.B. and Y.Y. performed the DFT and cRPA calculations. A.K. and S.A.J. contributed to the interpretation of the results. All authors discussed the results and contributed to the final manuscript.

Funding

Open Access funding enabled and organized by Projekt DEAL.

Competing interests

The authors declare no competing interests.

Additional information

Supplementary information The online version contains supplementary material available at https://doi.org/10.1038/s41524-025-01821-0.

Correspondence and requests for materials should be addressed to H. Hadipour or E. Şaşıoğlu.